
MODELLING INTERSTELLAR EXTINCTION IN STELLAR POPULATIONS

M.Phil. thesis

Alexander Lisboa-Wright

Astrophysics Research Institute, Liverpool John Moores University
September 2019

Abstract

Units & Terminology

Unless stated otherwise, all quantities will be described in CGS units (masses in grams, lengths in centimetres, times in seconds, energies in ergs).

In this project, the notation $\log(x)$ represents the logarithm of x to the base 10. The natural logarithm of x will be expressed as $\ln(x)$.

$$\begin{aligned}
 M &: \text{mass} \\
 M_{\odot} &= 1.989 \times 10^{33} \text{ g} : \text{solar mass} \\
 L &: \text{luminosity} \\
 L_{\odot} &= 3.842 \times 10^{33} \text{ erg s}^{-1} : \text{solar luminosity} \\
 g &: \text{gravity} \\
 R &: \text{radius} \\
 G &= 6.6723 \times 10^{-8} \text{ cm}^3 \text{ g}^{-1} \text{ s}^{-2} : \text{gravitational constant} \\
 \sigma_{\text{SB}} &= 5.678 \times 10^{-5} \text{ erg cm}^{-2} \text{ K}^{-4} \text{ s}^{-1} : \text{Stefan-Boltzmann constant}
 \end{aligned}$$

Chapter 1

Introduction

1.1 Extinction definition

As the light emitted from a star travels towards a distant observer, its intensity, or flux, f decreases with distance d via an inverse-square law:

$$f = \frac{L}{4\pi d^2} \quad (1.1)$$

where L is the star's luminosity, which is an intrinsic property of the star (i.e., independent of the observer). Equation 1.1 is a natural consequence of the same light wave expanding outwards from its source into a progressively larger spherical volume of empty space.

However, the interstellar medium is not a perfect vacuum. It contains many different structures, such as diffuse gas clouds, that can absorb or scatter light passing through, depending on the wavelength of the incoming photons, the spacing between the individual atoms (i.e., the density of the medium) and the quantum levels in the atoms occupied by their electrons. These absorption and scattering events are known as interstellar extinction. For a given source, its interstellar extinction coefficient represents the sum of the effects of all extinction events along the line-of-sight between the source and the observer.

Interstellar extinction preferentially affects light at shorter (i.e., bluer) wavelengths. Therefore, the effect of extinction is sometimes referred to as “reddening”, despite the fact that this term is also applied to a related, but distinct, quantity (see Section 1.7). Therefore, it should be expected that sources with proportionally higher fluxes at shorter wavelengths are most affected by extinction.

Extinction is defined using the standard astronomical system of flux magnitudes. In general, the difference between two flux measurements, f_1 and f_2 , in magnitudes, is expressed as:

$$m_1 - m_2 = -2.5 \log \left(\frac{f_1}{f_2} \right) \quad (1.2)$$

where m_1 and m_2 are the magnitudes for f_1 and f_2 , respectively. However, the flux of a source varies intrinsically with the distance travelled by the light to the observer (see Equation 1.1). To account for this, the distances to sufficiently close sources can be determined independently of their flux by measuring the sources' parallax from Earth.

The parallax p of an object is defined as the angular distance the object moves relative to the “fixed” background stars as the Earth moves a distance of 1AU (the average separation of the Sun and Earth during one complete orbit) perpendicular to the line-of-sight. This allows the distance, d , to be calculated using the geometry of triangles, combined with the small-angle approximation, as:

$$d/\text{pc} = \frac{1}{(p/\text{arcsec})} \quad (1.3)$$

For more distant stellar sources with much smaller parallaxes, a potential alternative is to view the object in a very long-wavelength filter, in which observations are likely to be impacted much less significantly by extinction, to estimate the type of star being observed, before using theoretical models to compare with observations at different wavelengths. This is more effective for brighter stars.

The role of distance gives each astronomical object two principal flux parameters. These are the apparent magnitude, m , and the absolute magnitude, M . The apparent magnitude is the flux magnitude of a source as observed by the telescope. The absolute magnitude is the predicted flux magnitude of the same source if it were to be placed at a fixed distance of 10 parsecs (pc) from the telescope with zero extinction. The absolute magnitude exists for the purpose of stellar classification, as the corresponding flux is simply a constant multiplied by the stellar luminosity (see Equation 1.1), which is an intrinsic physical property of the star.

However, to calculate the absolute magnitude of a source, we first require its distance and extinction coefficient, A . To account for extinction, it is necessary to define a new quantity, known as the intrinsic apparent magnitude, m_0 . This is defined as the flux magnitude of a source corrected for losses due to extinction but not due to distance. In practice, it represents the apparent magnitude for light passing through a fully-transparent medium. The relation between m_0 and M , can be found by combining Equations 1.1 and 1.2:

$$m_0 - M = -2.5 \log \left(\left(\frac{10\text{pc}}{d} \right)^2 \right) = 5 \log \left(\frac{d}{\text{pc}} \right) - 5 \quad (1.4)$$

This quantity is known as the distance modulus. As seen in Equation 1.4, it varies only with distance. The quantity $m - M$, linking the initial observed data with the

final theoretical data, is known as the apparent distance modulus and varies with both distance and extinction.

Therefore, the extinction coefficient A , defined as the flux lost due to the effects of the intervening line-of-sight medium, can be defined as:

$$A = m - m_0 \quad (1.5)$$

This fits with the physical definition of interstellar extinction given earlier, i.e. as the flux lost solely due to scattering and absorption in the interstellar medium.

1.2 Observational constraints

No telescope can view the sky at all spectral wavelengths - it would be wholly impractical due to the sheer number of sources across the spectrum, as well as the fact that telescope resolution depends on the wavelength of the incoming light. Therefore, modern telescopes are equipped with a system of filters or bands, which allow only light within a narrow range of wavelengths. In a filter system, the individual filters are designed to operate best at different wavelengths. The filter system therefore covers a much wider range of spectral wavelengths than a single filter would alone. This property is used to observe stars at different wavelengths to determine their spectral colour, which in turn grants further physical information about the star (see Section 1.7 for details).

Furthermore, the filters in a given system are designed such that the range of wavelengths in which each can detect incoming light overlaps with those of its neighbour(s), as shown in Figures 2.2-2.3. This ensures that there are no wavelength gaps in which incoming light cannot be detected. This is particularly important for quantum line emission, which occurs only at specific wavelengths for particular electron occupancy levels (see Section 1.5 for exceptions relevant to this project). One of the most prominent case of astrophysical line emission is that of $H\alpha$, in which the electron in a neutral hydrogen atom transitions from the $n = 3$ to the $n = 2$ quantum occupation state, emitting a photon with a wavelength of 656 nm, which is in the red part of the visible spectrum.

Filters, although necessary, therefore present an additional challenge when trying to determine stellar spectra accurately. This task is further complicated by the fact that, even in the wavelength range where a filter does detect incoming flux, the fraction of light it detects, known as the transmittance, is not uniform across the range. The transmittance as a function of wavelength is known as a transmission curve, bandpass or filter response function. Examples of response functions for filter systems employed in this project are shown in Figures 2.2-2.3. By comparing these with the filters' infor-

mation in Table 2.2, it can be seen that the exact shape of the response function could have a significant impact on the observed spectrum if not taken into account.

1.3 The standard treatment of extinction in observations

In observations, the extinction for a given source is initially unknown. For a stellar population, observers must make use of HR diagram features (absolute magnitudes) that vary as little as possible with variations in age and metallicity. The only known example of this is the red clump (Castellani et al., 1992), representing giant stars sustaining core helium burning. In the HR diagram, these stars form the red terminus of the horizontal branch (HB). Since the age and mass of a star at a given stage in its evolution correlate strongly, the location of the red clump is, by extension, also independent of the masses of its constituent stars. Paczyński & Stanek (1998).

The treatment of extinction in observational surveys is usually via a global extinction value for each filter, such as the constant A_X/A_V ratios given by Rieke & Lebofsky (1985). This approach has the significant issue of producing A_X values that do not account for star-to-star variations in flux, which can be several orders of magnitude. As shown in Figure 1.1, the monochromatic flux at a given wavelength varies greatly with effective temperature, as does the ratio between monochromatic fluxes of stars of different temperatures. This makes the notion that stars of different temperatures lose the same flux in a given filter passband, implied by using constant extinction ratios across all stellar classes, inherently flawed. Stars with higher effective temperatures have emission spectra with much higher and (proportionally greater) fluxes at the shorter wavelengths which are most impacted by interstellar extinction. Therefore, it should be expected that hotter stars experience higher extinctions A_X for a given filter, not equal values.

1.4 Empirical extinction curves

Rieke & Lebofsky (1985) found that outside dense molecular clouds, which have high opacities and whose lines-of-sight are less frequently used as a result, all extinction laws for all Johnson filters studied were uniform between wavelengths of 1 and 13 μm when observing sources in the direction of the Galactic Centre. This result was then used to produce constant A_X/A_V extinction ratios in the same filters. They also determined the now-widely used global average value of 3.08 (3.1) for $R_V = A_V/E(B - V)$, known as the total-to-selective extinction ratio, for the diffuse ISM.

Cardelli et al. (1989) used observations of mostly O- and B-type main-sequence

stars to produce empirical equations describing the mean ratio of extinction coefficients at a specific wavelength λ (A_λ) to the extinction in the Johnson- V filter (A_V), respectively. From this point onward, this ratio will be referred to as A_λ/A_V . They produced a basic equation of the form:

$$A_\lambda/A_V = a(x) + b(x)/R_V, \quad (1.6)$$

where $x \equiv 1/\lambda$ and $R_V \equiv A(V)/E(B-V)$. The significance of R_V , as noted in the same paper, comes from its usefulness as an indicator of the nature of the interstellar medium through which the observed light travels in order to reach the observer. The total wavelength range was divided into 4 sub-ranges, each with a governing pair of empirically-determined equations to calculate $a(x)$ and $b(x)$, respectively. This model underpins more recent studies of intrinsic effects on extinction (Girardi et al. (2008), Casagrande & Vandenberg (2018)), and provides the basis for the synthetic A_X/A_V datasets in this project. Equation 1.6 has become a standard model for theoretical studies to employ for predictions made in the UV, optical and near-IR wavelength regions, although it is not always accurate (O'Donnell (1994), Fitzpatrick (1999)).

O'Donnell (1994) found deviations from the Rieke & Lebofsky (1985) extinction law in the soft-UV spectral range using a sub-sample of 22 stars from the same dataset. This was attributed to the uncertainty in the short-wavelength cutoff of the UV-range Johnson U filter and to the presence of the Balmer discontinuity within the limits of the filter bandpass.

Fitzpatrick (1999) found that, due to the broadband nature of the Johnson filters and the general decrease of extinction with wavelength, the Cardelli et al. (1989) relations overestimate the extinction in the near-IR and blue-visible Johnson filters. The study put forward corrections to the equations for $a(x)$ and $b(x)$ for these wavelength regions. However, in the UV region covered by the Cardelli et al. (1989) equations, the equations are accurate for 93% of a homogeneous UV observational database (Valencic et al., 2004).

Girardi et al. (2008) produced data tables of A_X/A_V via bolometric corrections (as was carried out in this study). for stellar atmosphere models with parameters T_{eff} , $\log(g)$ and $[\text{Fe}/\text{H}]$. They carried this out using the same ATLAS9 data (Castelli & Kurucz, 2004) that was used to generate the data for this project, but also combined it with data from other studies Girardi et al. (2002), resulting in data covering a parameter space extending beyond the ATLAS9 limits in all three parameters. They used the data tables to calculate the A_X/A_V values for the stellar models in Padova theoretical isochrones. While determining that the values of A_X/A_V varied significantly with T_{eff} and $\log(g)$, the variation with metallicity was found to be 0.17% between $[\text{Fe}/\text{H}] = 0.0$ and $[\text{Fe}/\text{H}] = -2.5$. They found that, when they set $A_V = 6$, there was a systematic shift for the ACS system between extinction values calculated star-wise using the BC tables and a constant extinction value. The constant values of A_X/A_V were calculated

from a yellow dwarf in the low-extinction regime. Overall, the BC tables produced a smaller extinction coefficient in the F814W filter and a larger (F475W-F814W) colour index value. It also caused a change in the shape of the curve at the MSTO. They then applied the BC table data method to the case of the globular cluster M92. They found the optimal metallicity to be $Z = 0.0004$ ($[\text{Fe}/\text{H}] \approx -1.6$) instead of the value obtained by previous observers of $Z = 0.0001$ ($[\text{Fe}/\text{H}] \approx -2.2$). Therefore, their use of BC data caused the estimated cluster metallicity to be greater than when using the standard one-size-fits-all approach to extinction.

Casagrande & Vandenberg (2014, 2018a, 2018b) created simple linear models in multiple telescope filter systems, with the output parameter being $R_X = \frac{A_X}{E(B-V)}$. This was based on MARCS model stellar atmospheres, which have an upper T_{eff} limit of 8000K (Gustafsson et al., 2008). The equation is independent of surface gravity and has the following form:

$$R_X = a_0 + T_4(a_1 + a_2 T_4) + a_3 [\text{Fe}/\text{H}] \quad (1.7)$$

where $T_4 = 10^{-4} \times T_{\text{eff}}$. The equation is valid for $5250\text{K} \leq T_{\text{eff}} \leq 7000\text{K}$. Although these models are mathematically simple (with only 4 coefficients), the limited T_{eff} range in which they are applicable is problematic, particularly in the red giant branch and lower main sequence of any stellar population.

1.5 Stellar parameters affecting extinction

To understand the significance of differences between stars with respect to interstellar extinction, we must first define the fundamental features of a stellar atmosphere, which will be used in this project as the input variables on which any star-to-star variations in extinction will be modelled.

The effective temperature (T_{eff}) of a star is defined as the thermodynamic temperature of a black body which produces the same stellar flux across all wavelengths (known as the bolometric flux) as that produced by the star. The equation of the radiation emitted by a black body produces the body's flux per unit wavelength per unit angular viewing area, $F_{\lambda,bb}$, known as the black body's monochromatic flux. The equation, known as the Planck Law, is as follows:

$$F_{\lambda,bb} = \frac{2hc^2}{\lambda^5 \left(\exp\left(\frac{hc}{\lambda k_B T}\right) - 1 \right)} \quad (1.8)$$

where T is the thermodynamic temperature of the black body, h is Planck's constant, c is the vacuum speed of light and k_B is Boltzmann's constant. This equation also holds if the light wave frequency is used instead of the wavelength, with the monochromatic flux $F_{\nu,bb}$ now being the black body flux per unit frequency:

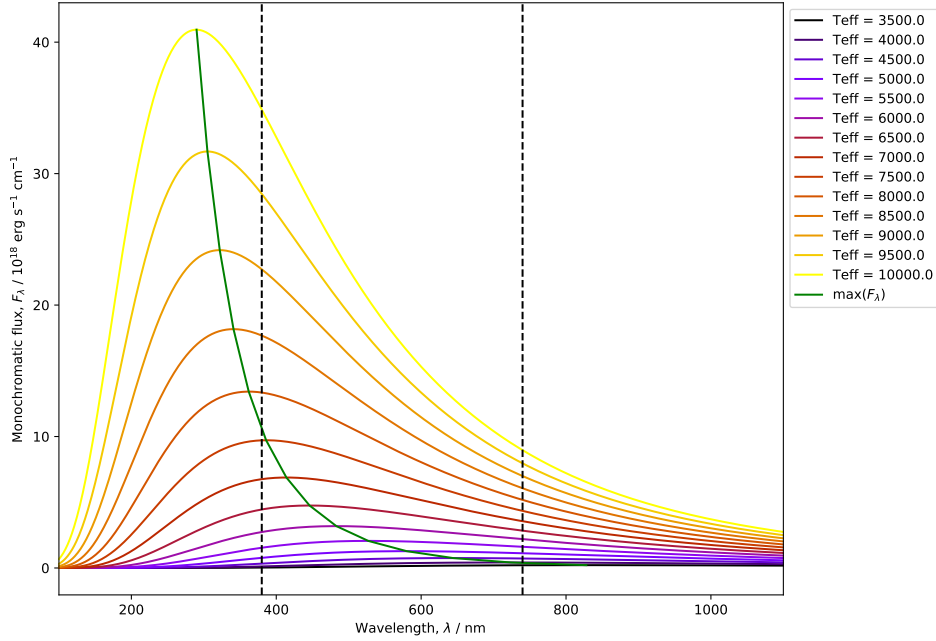


Figure 1.1: Monochromatic flux of a black body for different stellar effective temperatures. The black dashed lines mark the approximate limits of the visible part of the EM spectrum. The green curve represents the distributed of the maxima for the other curves.

$$F_{\nu,bb} = \frac{2h\nu^3}{c^2 \left(\exp\left(\frac{h\nu}{k_B T}\right) - 1 \right)} \quad (1.9)$$

In this project, the definition of monochromatic flux for any given object will be reserved exclusively for the flux per unit wavelength, F_λ , with any calculations involving black body fluxes using Equation 1.8.

The general approximation of stars to black bodies (and hence the actual stellar surface temperature to T_{eff}) is valid because all stars have been observed to have spectra that closely resemble those of black bodies, with the notable exception of atmospheric absorption lines. The (intrinsic) luminosity of a star is defined as:

$$L = 4\pi R^2 \sigma_{SB} T_{\text{eff}}^4 \quad (1.10)$$

where R is the (mean) stellar radius. Effective temperature has an effect on interstellar extinction due to its strong effect on the stellar luminosity and, hence, the flux. For a higher flux, more photons are likely to interact with the ISM, hence a higher extinction coefficient.

The metallicity of a star is defined as the fractional abundance of heavy elements, often approximated by iron (Fe) alone, relative to the star’s hydrogen (H) abundance, compared to that of the Sun. The abundances are determined by the strength of the elements’ characteristic atomic absorption lines in the stellar spectra.

$$[\text{Fe}/\text{H}] = \log \left(\frac{N_{\text{Fe}}}{N_{\text{H}}} \right) - \log \left(\frac{N_{\text{Fe},\odot}}{N_{\text{H},\odot}} \right) \quad (1.11)$$

For a generic atomic species E , N_E represents its number density. For stellar observations, N_E is measured at the surface. Since the output is logarithmic, a value of $[\text{Fe}/\text{H}] = 0$ indicates solar metallicity. An increase in metallicity would cause the corresponding absorption lines to be stronger, thus reducing the observable flux. An increased metallicity also implies an increase in abundance of sub-ferrous metals. The presence of more nuclear species, each with unique absorption line configurations, inevitably creates more observable lines, further increasing the apparent extinction in the spectral flux.

The definition of the stellar surface gravity g is simply the value of the standard Newtonian gravitational acceleration, applied to the stellar surface (the mass is the total stellar mass, M_* , and the distance is the stellar radius, R_*):

$$g = \frac{GM_*}{R_*^2} \quad (1.12)$$

A greater surface gravity, as can be inferred from Equation 1.12, represents a surface with a higher mass density. For stars, being self-gravitating, this infers a higher atomic number density. The effects of surface gravity upon the emitted stellar spectrum arise directly from the effect of atomic number density on the quantum properties of the interactions between the photons and atomic electrons.

When a particle absorption a photon, the absorption process is not instantaneous and therefore carries an uncertainty in the time taken for the process to be completed, with a corresponding uncertainty in energy due to the Heisenberg uncertainty principle. Across a large number of absorptions for the same initial electron state, the result is a spread in the energies of the absorbed photons. The associated emission line is therefore broadened by the multiple wavelengths of the photons. This is universal and referred to as “natural broadening”.

The impact of surface gravity arises via additional broadening effects upon these same absorption lines. When broadening effects are applied to an emission spectrum, such as a spectrum from a stellar surface, the result is that fewer photons pass through the surface, thereby reducing the surface flux seen by an outside observer.

1.6 ****Forbes effect

The Forbes effect occurs as a broadband beam of light, such as that passes through an extended partially-transparent medium, such as the Earth’s atmosphere or an interstellar gas cloud. It states that the greater the distance travelled by a light beam through the medium, the more penetrating the beam becomes (Forbes, 1842). The physical basis for this effect is that those photons in the original beam with wavelengths that make them the most likely to be absorbed or refracted are separated from the beam earlier. Therefore, as the beam travels through the medium, its constituent photons are progressively less likely to be separated. Since a higher fraction of its photons are retained as the distance through the medium increases, the beam is more penetrating (Ohvri et al., 1999).

The Forbes effect thus has an impact on the non-zero A_V value used in Equation 2.7 because if a uniform medium is assumed, as here, where R_V is held constant at the standard diffuse ISM value of 3.1 (Cardelli et al., 1989), a larger A_V value implies a longer path through the ISM, and thus a stronger Forbes effect. According to Girardi et al. (2008), any significant impact from the Forbes effect on the values of A_X/A_V occurs for a chosen $A_V \gtrsim 4$. They found that the effect was particularly strong for stars with $T_{\text{eff}} \lesssim 3000\text{K}$ and that, unsurprising, it became greater as the wavelength range covered by the filter response function increased.

1.7 Effects of extinction on interpreting stellar populations

The goal of this project is to compare different extinction treatments and the subsequent effect on the interpretation of observational cluster datasets. For any observational set of stars, the stars’ extinction coefficients will be completely unknown from the data alone. In order to compare observational and theoretical data, the most convenient approach is to add the (theoretical) extinction coefficient(s) to the theoretical dataset magnitudes (i.e., absolute magnitudes), before comparing to the distance-corrected observational data. As a result, the quantity from each dataset that is being compared is the absolute magnitude plus the extinction coefficient. If we label this quantity $M_{\text{ext},X}$ for a given filter, we can define it as:

$$\begin{aligned} M_{\text{ext},X} &= M_X + A_X \text{ (theoretical data)} \\ &= m - (m - M)_{X,0} \text{ (observational data)} \end{aligned} \tag{1.13}$$

However, as noted earlier, in astronomy it is not feasible to attempt observations by a single instrument at all wavelengths. Telescopes instead are purpose-built to study a single wavelength range within the full EM spectrum. Within this range, telescope

observation ranges are further divided by filters or passbands, one of which is placed on their aperture at any given observation time. As shown in Figures 2.3-2.2, any single filter X has a limited range of wavelengths for which it is able to detect flux. It can also be seen in these figures that the transmittance of the filter changes as a function of wavelength. These instrumental factors must be considered, in addition to the observational challenges of distance and interstellar extinction, in order to correctly analyse observation telescope data.

If we compare the individual black body spectra in Figure 1.1, it can be seen that the maximum monochromatic flux of the black body occurs at an increasingly shorter wavelength for objects with increasingly higher temperatures. This makes the object appear bluer to an observer. The relationship between the wavelength at which the monochromatic flux is maximal (λ_{max}) and the black body temperature is quantified by Wien's displacement law:

$$\lambda_{max}T = 2.898 \times 10^6 \text{ nm K} \quad (1.14)$$

More importantly, for two wavelength regions which are sufficiently far apart, the change in flux between the regions is always greater for stars with higher effective temperatures. Therefore, to measure a star's effective temperature, observers compare the star's observed flux in two filters operating at different wavelengths within the UV-IR wavelength range. The difference between the star's flux magnitudes in each of the two filters is then taken, with the flux in the redder filter being deducted from that of the bluer filter. This quantity is known as the colour index. For two filters X and Y , with X being bluer than Y , the colour index of observations made using those filters, $(X - Y)$, is defined as:

$$\begin{aligned} (X - Y) &= m_X - m_Y \\ &= (m_{X,0} - m_{Y,0}) + (A_X - A_Y) \\ &= (X - Y)_0 + E(X - Y) \end{aligned} \quad (1.15)$$

where $(X - Y)_0$ is the true or intrinsic colour index of the object and $E(X - Y) = A_X - A_Y$ is known as the colour excess, but can also be denoted in literature using the term "reddening". A major advantage of using the intrinsic colour index over absolute magnitudes is that it is completely independent of distance. The colour excess represents the effect of extinction on the observed colour index. Its importance arises from the prominence of the intrinsic colour index in determining effective temperature. Higher values of $(X - Y)$ indicate redder stars, with lower effective temperatures.

The most commonly-used colour index, employed as a reference for most optical observations, is the Johnson ($B - V$) index. This is due to these filters being the among most long-lived, well-used and best-studied available, allowing for better comparisons of different data, including data from older archives.

Due to the potential confusion due to the use of the term “reddening” for both A_X and $E(X - Y)$ in literature, A_X will be referred to here as the “extinction” or “extinction coefficient” and $E(X - Y)$ as the “colour excess”.

1.8 Project objective

The goal of this project is to attempt to use analytic functions to model the variation of the extinction coefficients in multiple photometric filter systems, across as large a range of stellar types as possible, with the ultimate goal of using this simplification of the variations to determine the differences in the estimated optimal ages, elemental abundances (known collectively in astronomy as metallicity) and extinction reference values of stellar populations (i.e., star clusters) from the current standard method for simulating extinction. If such differences exist and if they are of significant size, it could cause a recalculation of the properties of observed star clusters. This could potentially cause a reinterpretation of these clusters’ history, including where and when they formed in the Milky Way and the chemical enrichment of the gas that formed their stars.

Chapter 2

Methodology

2.1 Calculating extinction ratio data

All the equations in Section 1.7, including those for extinction, are not useful when applied to telescopes, as any filter will only detect a small fraction of the bolometric stellar flux that reaches the telescope. The missing information resulting from this observational constraint renders it difficult to determine the interstellar extinction. These constraints must be mitigated before an accurate value of the extinction coefficient can be determined. This mitigation is carried out by calculating corrections.

The use of bolometric corrections requires the detailed knowledge of stellar spectra least susceptible to significant extinction, i.e., nearby stars with high apparent fluxes. Only with complete knowledge of the spectrum from a reference star can the true spectrum of a distant star with unknown extinction be calculated. The spectra of these stars can be computed by using a grid of predicted fluxes from a stellar atmosphere model, the grid being composed of the stellar parameters known to change emission in stellar atmospheres. These are effective temperature, surface gravity and metallicity. For all filter systems studied in this project, the nearby bright star Vega (α Lyr) was used as the reference object. Using Vega as the reference star is the most well-known approach to photometric calibration (Casagrande & VandenBerg, 2014).

After accounting for the effect of interstellar extinction on an object's emission, its apparent magnitude in the wavelength range of a given filter X , defined as increasing from the shortest (λ_1) to the longest (λ_2) wavelength for which its response function is non-zero, can be calculated as:

$$m_X = -2.5 \log_{10} \left(\frac{\int_{\lambda_1}^{\lambda_2} f_{\lambda} (10^{-0.4A_{X,\lambda}}) S_{\lambda} d\lambda}{\int_{\lambda_1}^{\lambda_2} f_{\lambda}^0 S_{\lambda} d\lambda} \right) + m_X^0 \quad (2.1)$$

where f_{λ} represents the (theoretical) monochromatic flux at a given wavelength λ at the observer distance from the source, $A_{X,\lambda}$ is the extinction coefficient in X as

a function of wavelength and S_λ represents the filter response function of X . f_λ^0 and m_X^0 represent the monochromatic flux and apparent magnitude, respectively, in X of a known reference object, which is Vega in the case of this project.

To derive the equation linking a bolometric correction with the extinction parameter, we start with the definition of a bolometric correction in a filter X , which is denoted by BC_X :

$$BC_X \equiv M_{\text{bol}} - M_X \quad (2.2)$$

where M_X is the absolute magnitude of the object in X and M_{bol} is its (predicted) absolute bolometric magnitude, defined relative to the Sun using:

$$M_{\text{bol}} = M_{\text{bol},\odot} - 2.5 \log_{10} \left(\frac{4\pi R^2 F_{\text{bol}}}{L_\odot} \right) \quad (2.3)$$

where F_{bol} is the bolometric stellar flux at its surface, R is the stellar radius, $M_{\text{bol},\odot}$ is the solar absolute bolometric magnitude, which is assumed in this work to have a value of 4.75 and L_\odot is the solar luminosity, for which a value of $3.844 \times 10^{33} \text{ erg s}^{-1}$ is used. Bolometric corrections can be expressed as a function of extinction using the definition of M_X in terms of m_X and the distance d to the source:

$$M_X = m_X - 2.5 \log_{10} \left(\left(\frac{d}{10 \text{ pc}} \right)^2 \right), \quad (2.4)$$

together with the equation $f_\lambda d^2 = F_\lambda R^2$, where F_λ is the monochromatic flux at λ at the stellar surface. This gives the final function for a bolometric correction for filter X :

$$\begin{aligned} BC_X = M_{\text{bol},\odot} - m_X^0 - 2.5 \log_{10} \left(\frac{4\pi R^2 F_{\text{bol}}}{L_\odot} \right) \\ + 2.5 \log_{10} \left(\frac{\int_{\lambda_1}^{\lambda_2} F_\lambda (10^{-0.4A_{X,\lambda}}) S_\lambda d\lambda}{\int_{\lambda_1}^{\lambda_2} f_\lambda^0 S_\lambda d\lambda} \right) \end{aligned} \quad (2.5)$$

For a filter X , the extinction parameter $A_X = A_{X,\lambda}$ must be calibrated relative to a known value. In this work we will input a value of the extinction in the well-studied Johnson- V filter, A_V . To extract A_X , we use the simple relation:

$$A_{X,\lambda} = \left(\frac{A_{X,\lambda}}{A_V} \right) A_V \quad (2.6)$$

together with the chosen value of A_V (for this project the values were $A_V = 0, 1$ - note that $BC_X(A_V = 0)$ essentially assumes no extinction in any filter), before taking the difference between the two $BC_X(A_V)$ outputs, giving the following equation (Girardi et al., 2008):

$$BC_X(0) - BC_X(A_V) = (A_X/A_V) A_V \quad (2.7)$$

As demonstrated in the equation above, any dependence of the A_X/A_V data on the Vega measurements or (as yet unknown or uncertain) bolometric quantities from Equation 2.5 is eliminated during the subtraction.

Once the data A_X/A_V was calculated, analytical model templates of the three stellar parameters described in Section 1.5 were created and applied to the data, with the best-fit model coefficients being calculated using a least-squares fit algorithm.

2.2 Software used

To generate the predicted stellar flux, the ATLAS9 model stellar atmosphere code (Kurucz, 1993) was used to produce monochromatic fluxes for a series of wavelengths ranging from 9 nm to 160,000 nm, with a resolution of 2 nm or less in the UV. Table 1 of Castelli & Kurucz (2004) contains precise details of the coverage in $(T_{\text{eff}}, \log(g))$ parameter space, while a brief summary of the limits of the space is listed in Table 2.1. Four input metallicities were used for ATLAS9, at values of $[\text{Fe}/\text{H}] = -2, -1, 0$ and 0.5, covering the metallicities of most observed globular and open clusters. Each metallicity case was subject to the same coverage in ATLAS9. As shown in Figure 2.1, with the exception of the coolest, and therefore faintest, main sequence stars in the bottom right of the figure, the ATLAS9 grid covers the required parameter space for isochrones of all ages. The variation of isochrones at the plotted ages with metallicity is not significant with respect to the grid coverage.

The tables of bolometric corrections were generated using a FORTRAN 77 code incorporating the steps described in Section ??, inputs with tables describing the response functions of all three filter systems at the same wavelengths as those listed in the ATLAS9 model atmosphere tables, with the number of tables for each stellar metallicity value equal to the total number of $(T_{\text{eff}}, \log(g))$ combinations available.

Once the bolometric correction tables were produced, all subsequent processes were written in Python 2.7 in the form of an IPython notebook. The repository containing all data, plots and programme codes for this project can be found at https://github.com/AlexlwAstro/phd_work.

The isochrones used were generated using the latest Bag of Stellar Tricks and Isochrones (BaSTI) web interface (Pietrinferni et al. (2004), Hidalgo et al. (2018)). The filter systems whose throughput data were employed by BaSTI to generate the fluxes for the isochrones were ACS, WFC3 and Gaia-DR2. It should be noted that the

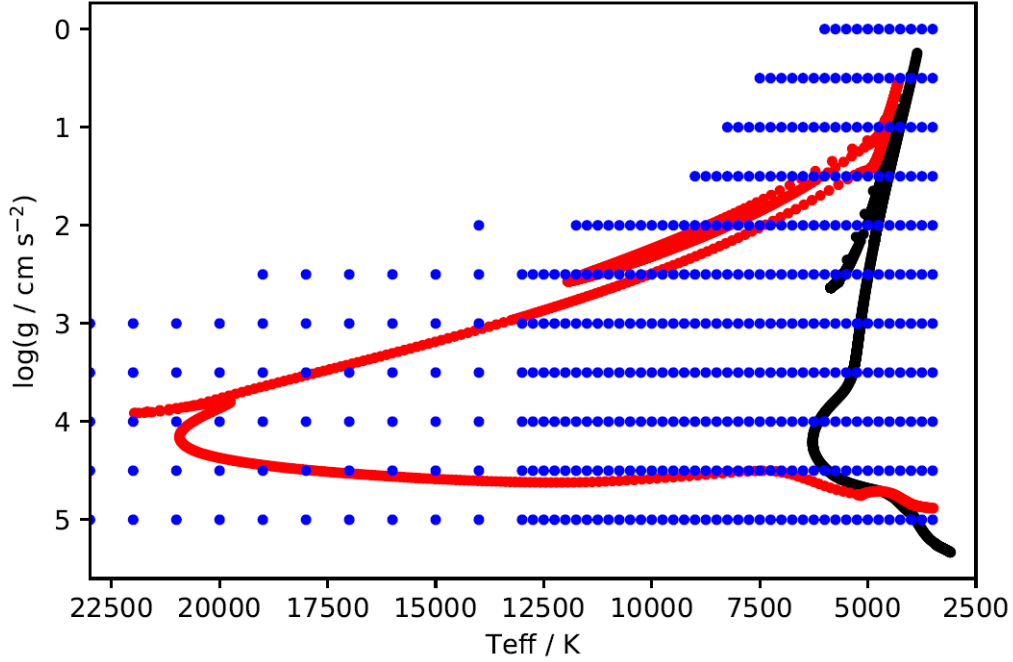


Figure 2.1: $T_{\text{eff}}\text{-log}(g)$ scatter plot for a BaSTI 50 Myr, $[\text{Fe}/\text{H}] = -1$ isochrone (red), a BaSTI 12 Gyr, $[\text{Fe}/\text{H}] = -1$ isochrone (black) and ATLAS9 model grid (blue) for $T_{\text{eff}} \leq 23000$ K.

Parameter / unit	Minimum	Maximum	Number of values
$T_{\text{eff}} / \text{K}$	3500	50000	76
$\log(g / \text{cm s}^{-2})$	0.0	5.0	11
$[\text{Fe}/\text{H}]$	-2.0	0.5	4

Table 2.1: Ranges for the input parameters for ATLAS9 atmospheric models

WFC3 isochrone output for BaSTI does not include flux magnitudes for the F300X filter.

2.3 Filters studied

In this project, three broad-band filter systems were employed. Two are systems on board the Hubble Space Telescope (HST). These are the Advanced Camera for Surveys (ACS), installed in 2002 on the HST (Sarajedini et al., 2007), and the Ultraviolet Imaging Spectrograph channel of the Wide-Field Camera 3 (WFC3/UVIS), installed on the HST in 2009 (Kalirai et al. (2010), MacKenty et al. (2010)). The third is the single set of three broadband filters mounted on the Gaia space observatory (Jordi et al., 2010), launched in 2013.

Reference will also be made to the Johnson-Morgan filter system (often simply known as the Johnson system) UBV Johnson & Morgan (1953), later extended as the Johnson-Cousins UBVRI Bessell (1990) system, which has been in use for decades and continues to be the standard reference for more modern filter systems. Of particular importance are the Johnson blue (B) and yellow (V) filters, as these formed the original benchmark for observing stellar populations and evolutionary stages.

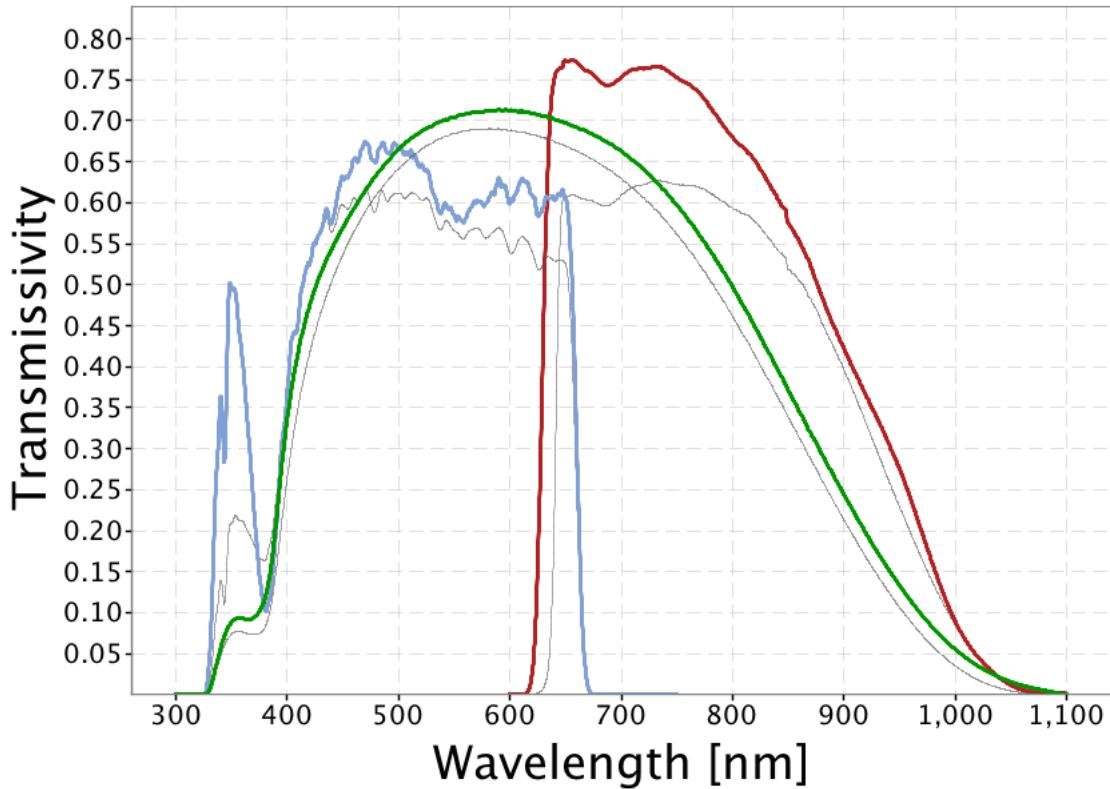


Figure 2.2: Filter response functions for Gaia photometric filters. Source: https://www.cosmos.esa.int/web/gaia/iow_20180316

The standard treatment of extinction is to apply a single constant value of the extinction coefficient for a given filter X , denoted in the literature by A_X . For wavelengths in or around the optical spectral range, this quantity is usually expressed as a fixed ratio of the (constant) coefficient value in the Johnson- V filter, the standard visual comparison filter. The wavelengths of optical light typically range between 3800 Å and 7400 Å.

In Table 2.2, all the filters used for this project are listed. The name of each filter is displayed alongside its central wavelength (λ_{cen}), full-width at half-maximum (FWHM) and the minimum (λ_{min}) and maximum (λ_{max}) detection wavelengths. Hence, when

System	Filter	$\lambda_{\text{cen}} / \text{\AA}$	FWHM / \AA	$\lambda_{\text{min}} / \text{\AA}$	$\lambda_{\text{max}} / \text{\AA}$
ACS	F435W	4359	881	3610	4860
	F475W	4781	1403	3863	5563
	F555W	5413	1236	4584	6209
	F606W	5961	2255	4634	7180
	F625W	6323	1390	5446	7100
	F775W	7763	1517	6804	8632
	F814W	8117	2096	6885	9648
WFC3	F218W	2216	329	1990	2603
	F225W	2341	464	1990	2968
	F275W	2696	417	2282	3119
	F300X	2722	660	2137	4098
	F336W	3368	550	3014	3707
	F390W	3929	951	3255	4470
	F438W	4322	674	3895	4710
	F475W	4768	1482	3942	5582
	F555W	5262	1578	4381	7045
	F606W	5941	2298	4700	7204
	F625W	6274	1573	5414	7138
	F775W	7725	1454	6869	8571
	F814W	7814	1505	6978	9684
Gaia	G	6631	4397	3321	10515
	G_{bp}	5330	2530	3283	6714
	G_{rp}	7896	2956	6296	10637

Table 2.2: Basic properties of the filters employed in this project. See text for details. Source: <http://svo2.cab.inta-csic.es/svo/theory/fps3/index.php>

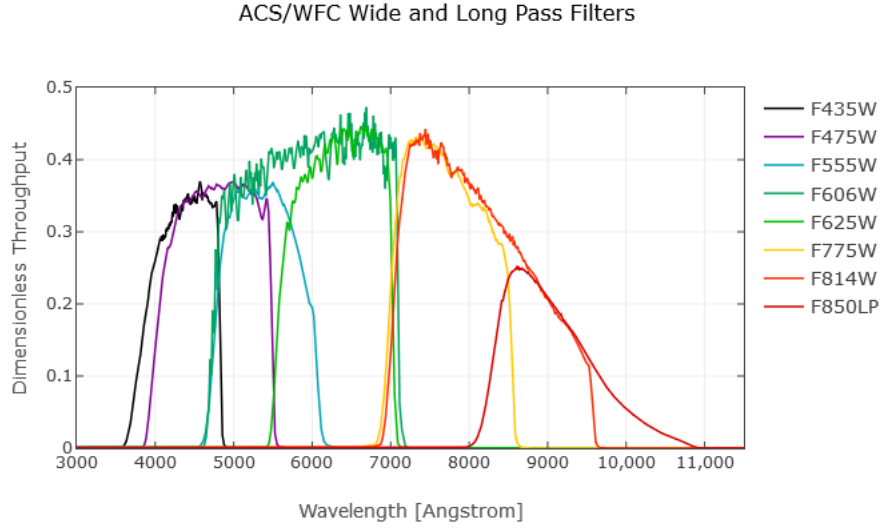


Figure 2.3: Filter response functions for wide-field ACS filters. Source: <http://www.stsci.edu/hst/acs/analysis/throughputs>

combined, these filters cover wavelengths from the soft-ultraviolet (soft-UV) to the near-infrared (NIR), including all visible wavelengths. The FWHM is defined as the difference between the lowest and highest wavelength values at which the transmittance value is half of its maximum value for the filter, typically assuming the response function can be approximated as a Gaussian distribution centred on the central wavelength. The FWHM acts as an approximate measure of the wavelength range within which the filter can reliably be used for observations.

2.4 Isochrone data fitting

To obtain isochrones from the BaSTI online database, the desired age range, initial metallicity and filter system must be specified. Therefore, the values of these quantities are shared by all stellar objects. For the stages in stellar evolution prior to the main-sequence turn-off, any changes in atmospheric metallicity are insignificant, due to the factors discussed in Section ??.

The output from the BaSTI database for each model stellar object gives the model's initial mass and current mass (i.e. after a time equal to the isochrone age), together with the logarithms of the stellar luminosity in solar units ($\log(L/L_{\odot})$) and of the effective temperature in K ($\log(T_{\text{eff}})$), followed by the absolute magnitudes (with zero extinction) of the object in each filter of the system. To derive the surface gravity g , we

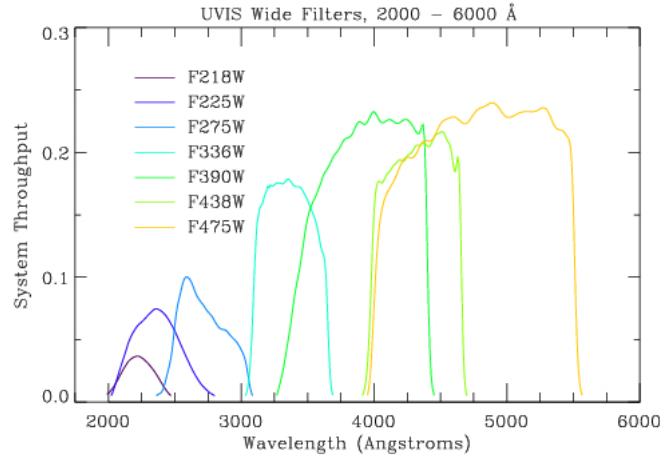


Figure 2.4: Filter response functions for wide-field WFC3 filters. Source: http://www.stsci.edu/hst/wfc3/ins_performance/throughputs/UVIS_filterthru.html

Isochrone (Age/Myr , [Fe/H])	T_{eff} minimum	T_{eff} maximum	$\log(g)$ minimum	$\log(g)$ maximum
500,0.002	2870	9640	0.886	5.137
1000,0.002	2824	8035	1.608	5.184
5000,-1.049	3118	7112	0.456	5.318
10000,-1.049	3086	6412	0.286	5.332

Table 2.3: Ranges of effective temperature and surface gravities in selected BaSTI isochrones

must combine Equation 1.10, to derive the stellar radius, and Equation 1.12. Equation 2.8 shows the resultant definition of g :

$$g = \frac{4\pi GM_* \sigma_{\text{SB}} T_{\text{eff}}^4}{L_*} \quad (2.8)$$

After this had been completed, each object had a co-ordinate in $(T_{\text{eff}}, \log(g))$ parameter space, plus the metallicity of the overall isochrone model. The filter magnitudes in the photometric data are the apparent magnitudes of the stars assigned to NGC 6793. Therefore, to match the quantities of the observational and isochrone datasets being compared, it was necessary to correct the observational data for distance and add extinction to the isochrones. This is that standard procedure used when analysing observational data. Thus, we were comparing the $M_{\text{ext},X}$ values for the isochrones and the observational data. The functions described in Section 3.3 were then applied to the dataset of stellar objects, producing values of $M_{\text{ext},X}$ for each filter for all objects, as is the standard for analysing observational data with unknown extinction coefficients.

When comparing the two approaches to extinction, in order to test for any differ-

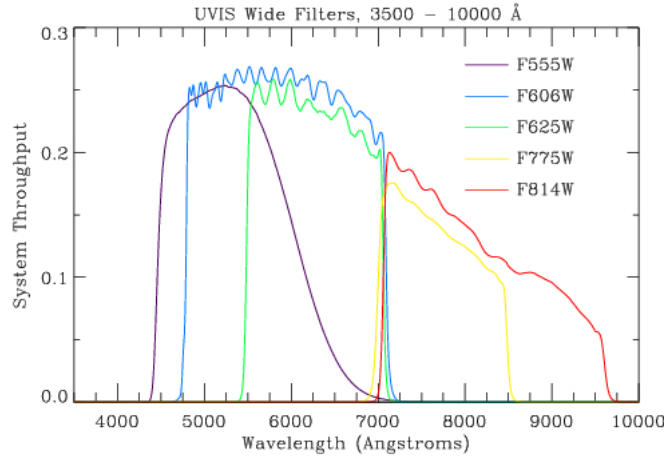


Figure 2.5: Filter response functions for wide-field WFC3 filters. Source: http://www.stsci.edu/hst/wfc3/ins_performance/throughputs/UVIS_filterthru.html

ences in projected isochrone age via the MSTO, a range of ages must be considered. A “primary” age was utilised as the true cluster isochrone age. This primary isochrone was subjected to both the function-based (FBEC) and standard extinction-coefficient approaches. Two isochrones with ages equidistant from the primary were subjected to the standard approach only. All four of the resulting $M_{\text{ext},X}$ isochrones were plotted together in the four chosen CMD axes, together with the original (zero-extinction) isochrone for visual reference.

This procedure was employed for two values of A_X/A_V for the standard (fixed) extinction treatment. Both were extracted from the ATLAS9 data tables for a $\log(g)$ value of 5.0 to represent a main-sequence star, highly desirable when comparing MSTO positions. Given the large number of filters studied in this project, four commonly-used CMD axes were selected to test for any effects of a function-derived A_X . Two of these are specific to the WFC3 system, with one CMD each for ACS and Gaia.

2.5 Observational test case: NGC 6793

To test the effects of the two different treatments of A_X/A_V on observational data, both were employed to predict the isochrone parameters (age, $[\text{Fe}/\text{H}]$ and A_V) for the open cluster NGC 6793.

NGC 6793 has little information available in the literature when compared to open clusters. Two observational studies have been published which give estimates for the properties of the cluster. Both sets of results are listed in Table 2.4.

The Gaia DR2 dataset for NGC 6793, containing the parallaxes and apparent mag-

Cluster property	K05	GC18
Distance modulus / mag	10.73	8.894
-> distance / pc	1400	601
log(age / yr)	8.64	8.78
-> Age / Myr	437	603
$E(B - V)$ / mag	0.17	0.843
-> A_V / mag (if $R_V = 3.1$)	0.53	0.682
$[Fe/H]$?	?
Members	? (> 3 ACSS-2.5)	465 (271 with Gaia photometry)

Table 2.4: Observational parameters for NGC 6793, according to Kharchenko et al. (2005) (WEBDA archive page) and Gaia Collaboration et al. (2018)

nitudes (in all three Gaia filters) for 338 objects identified as belonging to the cluster, was obtained. The number of objects is greater than the 271 photometric Gaia objects found by Gaia Collaboration et al. (2018), hereafter referred to as GC18. Restrictions on the parallax measurements were implemented, by imposing a distance-based selection range centred at 600 pc, which was treated as the centre of the cluster, in line with the GC18 estimate in Table 2.4. The range was decreased until the remaining sample size was approximately equal to 271. When this was implemented, the final sample of observational data for NGC 6793 contained 274 objects. Some of these objects still had parallax distances further from the cluster centre than would be expected for any star cluster. The size of the final dataset balanced the need for maintaining sufficient data points, to achieve a valid comparison to the previous studies of NGC 6793, particularly GC18, and eliminating the most anomalous data, such as stars with parallaxes calculated as being negative (and therefore not physically feasible).

The isochrone fitting to the NGC 6793 was done by eye using a plot of the cluster’s observed Gaia CMD, the position of each star corrected for its parallax distance. Using the values of $E(B - V)$ and age from GC18, a standard-case isochrone was derived, again assuming a diffuse ISM (i.e., $R_V = 3.1$). The standard treatment was employed twice, creating a different isochrone each time. A coefficient calculated from $(A_X/A_V)_{MS}$ was applied in one case and one calculated using $(A_X/A_V)_{plat}$ in the other. The fitting process was carried out in sequential stages:

1. First, the upper main sequence of the FBEC isochrone was fitted to that of the standard-case isochrone by varying the value of A_V used to calculate the final FBEC value for each stellar object.
2. Next, the age of the FBEC isochrone was varied to match the observed turn-off location in the NGC 6793 data as far as possible.
3. Finally, the FBEC isochrone metallicity was varied in an attempt match the

observed lower main-sequence.

The isochrone with the resulting parameters were then plotted alongside two standard-case isochrones, The resulting curves were compared to each other for accuracy with respect to the observational data.

Chapter 3

Results and discussion

3.1 Choice of R_V and A_V values

In order to generate the bolometric correction data, the Fortran software required the user to input a single, global value for the parameters R_V and A_V . The global R_V value, which is applied to the Cardelli et al. (1989) extinction law, was chosen as $R_V = 3.1$. This is equal to the mean diffuse ISM value calculated by Rieke & Lebofsky (1985) and widely used in analysis of stellar observations. The choice for the non-zero value of A_V was required in order to generate the A_X/A_V data via Equation 2.7. The choice for this global value was made as $A_V = 1.0$. This was chosen for multiple reasons:

- The value is sufficiently large for differences between both BC datasets to become apparent in the A_X/A_V data.
- The A_V values of observed stellar populations are often around or less than 1.0, which precludes using a higher value for the BC data.
- A value of $A_V = 1.0$ is also sufficiently small for the Forbes effect (see Section 1.6 to have a negligible impact, even for filters with the widest bandwidths.

3.2 Trends in A_X/A_V data

For all filters, the greatest variations in A_X/A_V data occur with changes in T_{eff} , with changes due to $\log(g)$ and $[\text{Fe}/\text{H}]$ being much less significant. Another general feature is the convergence of A_X/A_V to a single maximum value in each filter, at $T_{\text{eff}} = 50,000$ K, for higher effective temperatures, independent of metallicity and surface gravities. In most filters, this convergence is achieved to within a margin of 0.01 from the value at $T_{\text{eff}} = 50,000$ K by temperatures of 20,000 K. The region of parameter space in T_{eff} , $\log(g)$ and $[\text{Fe}/\text{H}]$ characterised as having achieved this convergence is referred to henceforth as the “high- T_{eff} plateau region” or simply “plateau”.

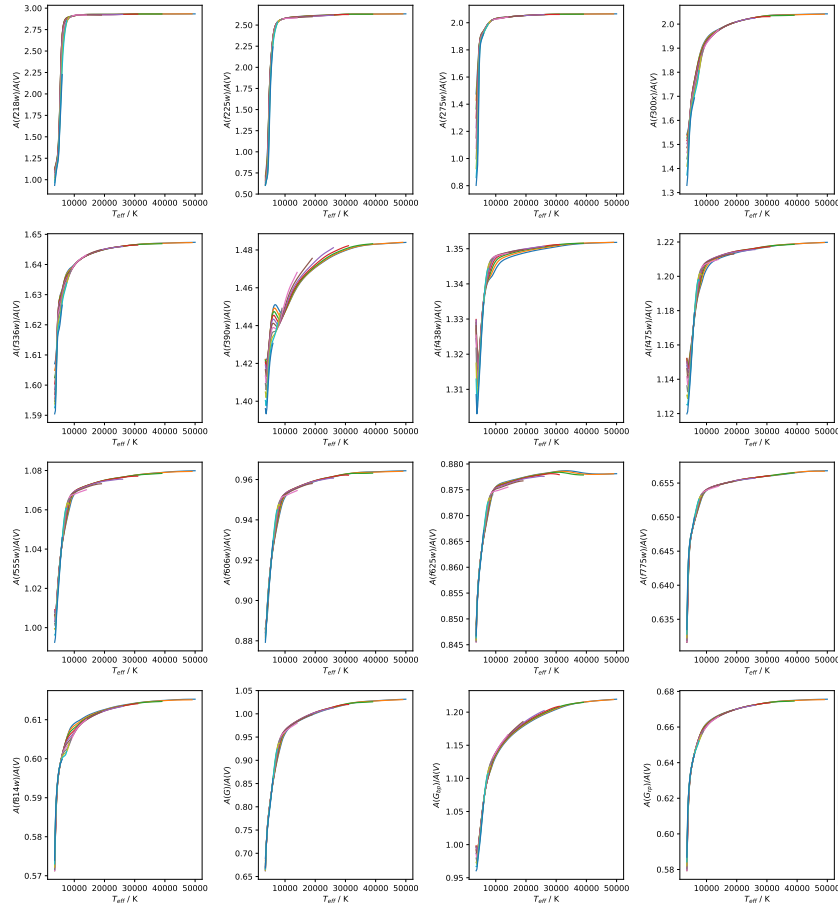


Figure 3.1: Solar-metallicity extinction ratio data for the WFC3 (first 13 panels) and Gaia (last 3) systems, with point-to-point lines connecting datapoints for a fixed $\log(g)$ value.

A property found in the data for some filters, more pronounced at higher metallicity but with a possible slight dependence on surface gravity, is the tendency of the gradient of A_X/A_V with increasing T_{eff} to become significantly less positive at the lowest temperatures in the data, typically around 4000K and below. The spread in A_X/A_V values for different $\log(g)$ is typically about 0.2-0.4, with a linear progression from $\log(g) = 5.0$ at the lowest end to $\log(g) = 0.0$ at the highest. In some filters, at the highest metallicity employed ($[\text{Fe}/\text{H}] = 0.5$), this phenomenon causes the gradient to invert and become significantly negative, reversing the trend everywhere else in the data, including for the same filters at lower metallicity. Due to the shape of the resulting point-to-point line in these axes, it has been dubbed the “tail-flick” phenomenon.

This gradient inversion was ignored as an artefact from the numerical integration required for Equation 2.5. This was justified on the basis that it is physical infeasible for a cooler star to experience a higher extinction A_X than a hotter star for a

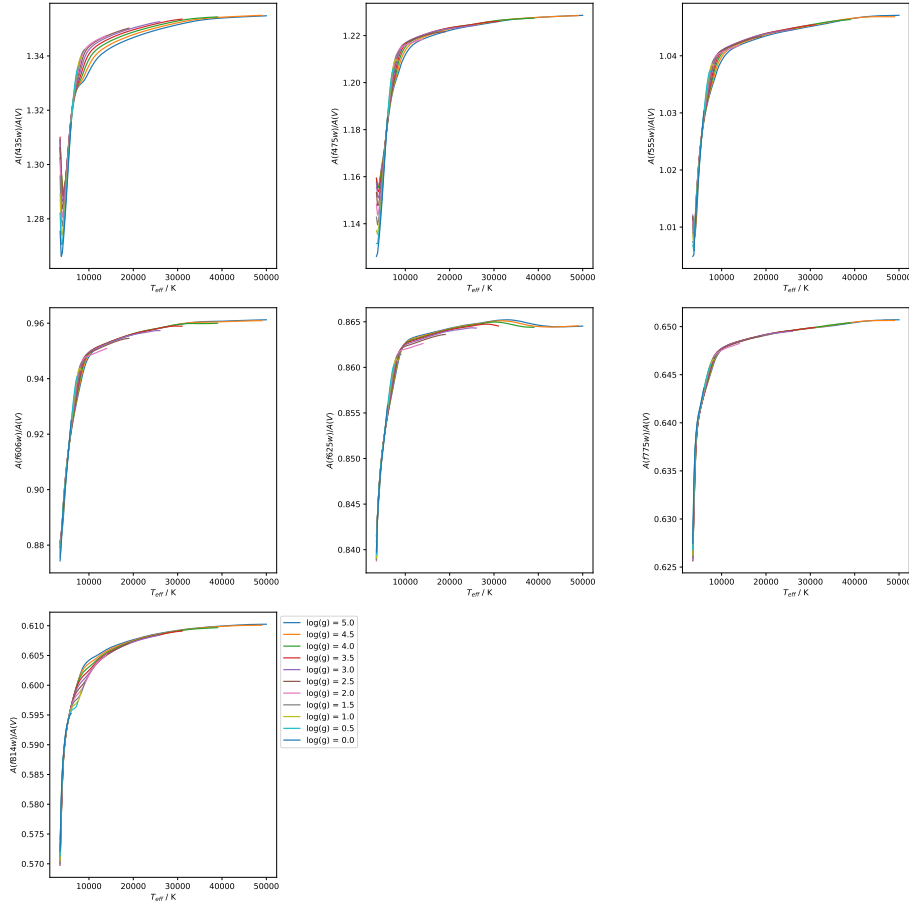


Figure 3.2: Same as Figure 3.1, except the filters shown here are for the ACS system.

globally-constant A_V value and metallicity, as was assumed for data in each BC table. In the relevant filters, only effective temperatures above those affected by the gradient inversion was used for fitting.

3.3 Extinction ratio models

In order to find usable model functions without running into issues with degeneracy between coefficients in the same function, prioritising the order in which the three stellar parameters were model was paramount. Too many coefficients created errors that were significantly greater in degenerate coefficients than in non-degenerate ones. This would obscure any useful information about the validity of the function form.

The bolometric flux of a black body can be calculated as the total area under the curve described by the Planck function per unit wavelength/frequency as a function of

wavelength/frequency (see Equations 1.8 and 1.9). Since stellar emission spectra can be reasonably approximated by a black body emission with absorption lines, it can be seen from Equation 1.10 that the greatest effect on stellar spectra, and therefore on the extinction coefficient, will come from changes in effective temperature. Therefore, the initial functions to be fitted were simple analytical functions of T_{eff} only:

$$A_{\text{pow}}(T_{\text{eff}}) = a(T_4)^b + c \quad (3.1)$$

$$A_{\text{exp}}(T_{\text{eff}}) = a \exp(bT_4) + c \quad (3.2)$$

where $T_4 = 10^{-4} \times T_{\text{eff}}$. The fitting operation was carried out on the data for solar metallicity ($[\text{Fe}/\text{H}] = 0.0$) and, because it gave the greatest number of T_{eff} data points, $\log(g) = 5.0$. This dataset will be referred to as the basic fitting data (BFD).

For the data in the Gaia filters, the opportunity was taken to compare the models produced in this project with the models for R_X for these same filters detailed by Casagrande & Vandenberg (2018). To apply the Casagrande & Vandenberg (2018) model to the extinction ratios used for this project, the definition of R_X was used to construct the following equation:

$$\frac{A_X}{A_V} = \frac{R_X}{R_V} = \frac{R_X}{3.1} \quad (3.3)$$

There were filters whose BFD could not support an accurate fit or maintain the desired accuracy across all combinations of $\log(g)$ and $[\text{Fe}/\text{H}]$ using A_{pow} or A_{exp} . For these filters, more intricate functions were sought, including functions with explicit dependences on g and $[\text{Fe}/\text{H}]$. Several unsuccessful approaches were made before an acceptable function was found for each filter. These included:

- Using a polynomial fit for the BFD, for filter which could not be accurately described in the BFD in the first instance.
- Fitting the entire dataset in two steps, by fitting the residuals from the A_{pow} and A_{exp} fitting processes to a new function with explicit variations in all three stellar parameters. The ****functions included damped-oscillator functions and oscillating power-law functions, among others. When fitted to the residuals, this meant an oscillation with amplitude decaying with increasing T_{eff} ****

The most successful approach was plotting all the available data for each filter, in multiple 2D and 3D axes, and analysing it visually. The trends seen in the data were transcribed to find not only an overarching function template, akin to the status of A_{pow} and A_{exp} , but also smaller mathematical constructs within the template, such as describing a decay coefficient in terms of $\log(g)$ and $[\text{Fe}/\text{H}]$. The details of the final form of the template as a function of each stellar parameter were deduced by fitting a logistic function of T_{eff} to the A_X/A_V data for each ($[\text{Fe}/\text{H}], \log(g)$) combination. This

was decided on the basis that A_{exp} had been superior to A_{pow} in describing the data for all relevant filters and because, for these filters, the low- T_{eff} change in gradient appeared to be more significant than for others and the gradient was not inverted, as can be seen in Figures ??-??. This is still the case, even after accounting for the difference in A_X/A_V scale between filters. In particular, the T_{eff} gradient prior to the plateau appears to lead to an asymptote at lower, but still physically-viable, temperatures. This issue is resolved by the logistic function's property of converging to a constant value for both very high and low values of the input variable.

For a general logistic function in T_{eff} , there are four principle parameters:

- The global maximum value, denoted in this case by A_{max} ;
- The global minimum value, A_{min} ;
- The exponential decay coefficient, k ;
- The T_{eff} -coordinate of the sigmoid midpoint, in this case T_0 .

It was confirmed that this new function could describe each scenario accurately enough for further analysis. The resulting coefficients were tabulated and analysed for trends and, if found, the nature of those trends. This allowed for the incremental construction of sub-functions of $\log(g)$ and $[\text{Fe}/\text{H}]$, making the overall function, A_{logis} , sensitive to all three input stellar atmosphere parameters, with effective temperature having the greatest effect and the relative effects of the other parameters dependent on the best-fit values of the relevant coefficients.

The sub-functions of $\log(g)$ and $[\text{Fe}/\text{H}]$, upon inspection of the coefficients for the T_{eff} -only logistic function, were found to be simple functions of $\log(g)$ and $[\text{Fe}/\text{H}]$, independent of T_{eff} variations. This allowed for them to be used as the definitions of T_0 and k , as shown in Equations 3.4 and 3.5, respectively.

$$T_0 = a \log(g) + b \left(\frac{[\text{Fe}/\text{H}]}{|[\text{Fe}/\text{H}]|^{1/2}} \right) + c \quad (3.4)$$

$$k = d \log(g) + e [\text{Fe}/\text{H}] + f \quad (3.5)$$

$$A_{\text{logis}}(T_{\text{eff}}, g, [\text{Fe}/\text{H}]) = \frac{(A_{\text{max}} - A_{\text{min}})}{(1 + \exp(-10^{-4}k(T_{\text{eff}} - T_0)))} + A_{\text{min}} \quad (3.6)$$

The final form was then subjected to a final fit on the entire A_X/A_V dataset, covering the entire $(T_{\text{eff}}, \log(g), [\text{Fe}/\text{H}])$ parameter space available. A_{logis} was able to accurately reproduce the behaviour of almost the entire dataset. The coefficients for Equations 3.4-3.6 are given in Table 3.2. ****

System	Filter	Function (A_{pow} or A_{exp})	Coefficients			(g)
			a	b	c	
ACS	F435W	exp	-0.144 ± 0.031	-2.159 ± 0.360	1.352 ± 0.002	
	F475W	exp	-0.214 ± 0.047	-2.660 ± 0.380	1.226 ± 0.002	
	F555W	exp	-0.0914 ± 0.048	-2.677 ± 0.901	1.045 ± 0.002	
	F606W	exp	-0.218 ± 0.055	-2.867 ± 0.445	0.959 ± 0.002	
	F625W	exp	-0.072 ± 0.078 -3.332 ± 2.000	0.865 ± 0.002	$3500(0.01)$	
	F775W	pow	-0.0035 ± 0.0042	-1.4878 ± 1.5414	0.6507 ± 0.0031	
	F814W	pow	-0.007 ± 0.0046	-1.3743 ± 0.8303	0.6108 ± 0.0034	
WFC3	F336W	pow	-0.0074 ± 0.0041	-1.5251 ± 0.7272	1.6478 ± 0.003	
	F390W	exp	-0.0695 ± 0.0057	-0.6438 ± 0.177	1.489 ± 0.005	
	F438W	exp	-0.1132 ± 0.0658	-3.0839 ± 1.0322	1.3504 ± 0.0017	
	F475W	pow	-0.0179 ± 0.0037	-1.718 ± 0.275	1.220 ± 0.003	
	F555W	pow	-0.0138 ± 0.0033	-1.8873 ± 0.3326	1.0798 ± 0.0024	
	F606W	exp	-0.2131 ± 0.0559	-2.8788 ± 0.4604	0.9623 ± 0.0017	
	F625W	pow	-0.0042 ± 0.0031	-2.0634 ± 1.0248	0.8787 ± 0.0022	
	F775W	pow	-0.0033 ± 0.0041	-1.529 ± 1.6335	0.6568 ± 0.003	
	F814W	pow	-0.0071 ± 0.0046	-1.3905 ± 0.8027	0.6158 ± 0.0034	
Gaia	G	pow	-0.0888 ± 0.0045	-1.402 ± 0.0642	1.0395 ± 0.0033	
	G _{bp}	pow	-0.115 ± 0.0081	-0.8997 ± 0.0692	1.2468 ± 0.0068	
	G _{rp}	pow	-0.0159 ± 0.0047	-1.3519 ± 0.3678	0.6772 ± 0.0035	

Table 3.1: Coefficient values produced for each filter via A_{exp} or A_{exp} fitting, as appropriately labelled. Any filters missing from this table are those with data that could not be accurately fitted using either function. The errors are calculated using a simulated A_X/A_V uncertainty of 0.01

The extinction-ratio data for all filters, with the exception of the four fully-UV filters in the WFC3 system, could be accurately modelled by the simplest functions trialled for fitting, $A_{\text{exp}}(T_{\text{eff}})$ or $A_{\text{pow}}(T_{\text{eff}})$.

f218w filter R1 [Fe/H]-log(g) logistic fit coefficients: [-1.2108e+02 4.4719e+02 5.6980e+03 1.4584e+00 -3.1737e+00 1.8991e+01 1.0257e+00 2.9087e+00] Standard deviation (square root of CM leading diagonal): [4.1046e+00 7.4523e+00 1.6317e+01 2.0969e-01 3.7843e-01 6.2261e-01 1.1639e-02 2.7489e-03]

**** f218w filter: calculating coefficients & covariance matrices for original data R1 [Fe/H]-log(g) logistic fit coefficients: [-1.2126e+02 3.9420e+02 5.7167e+03 1.4027e+00 -2.8642e+00 1.8734e+01 1.0227e+00 2.9087e+00] Standard deviation (square root of CM leading diagonal): [4.1130e+00 6.6376e+00 1.6523e+01 2.0731e-01 3.5276e-01 6.2525e-01 1.1756e-02 2.7509e-03]

Finished input array checks**** f225w filter: calculating coefficients & covariance matrices for original data R1 [Fe/H]-log(g) logistic fit coefficients: [-9.7567e+01 3.0315e+02 4.9975e+03 -1.3770e-01 -2.4579e+00 1.8018e+01 3.2623e-01 2.5811e+00] Standard deviation (square root of CM leading diagonal): [3.8466e+00 6.7860e+00 2.2584e+01 1.3365e-01 2.4018e-01 5.4534e-01 2.8243e-02 2.7531e-03]

Finished input array checks**** f275w filter: calculating coefficients & covariance matrices for original data R1 [Fe/H]-log(g) logistic fit coefficients: [-2.4029e+02 1.9525e+02 4.1111e+03 -1.8204e+00 -2.1289e+00 2.0441e+01 2.9592e-01 2.0308e+00] Standard deviation (square root of CM leading diagonal): [1.2301e+01 2.0185e+01 9.6566e+01 3.0954e-01 4.1540e-01 1.4140e+00 1.4197e-01 2.6803e-03]

Finished input array checks**** f300x filter: calculating coefficients & covariance matrices for original data R1 [Fe/H]-log(g) logistic fit coefficients: [-3.0161e+02 2.8717e+02 4.3008e+03 -1.7560e-01 -3.3813e-01 4.2631e+00 1.0000e+00 2.0144e+00] Standard deviation (square root of CM leading diagonal): [4.4848e+01 1.1124e+02 9.2578e+02 8.7242e-02 1.0762e-01 5.2855e-01 1.9919e-01 4.3986e-03]

All the functions are consistent with the general trends predicted by the physics in stellar atmospheres, since the effective temperature has the greatest effect upon the value of A_X/A_V , with relatively minor effects due to spectral absorption lines, via surface gravity and metallicity. In general stars with higher effective temperatures (and consequently stronger and bluer flux spectra) experience higher A_X/A_V values in all filters than stars with low effective temperatures. The maximum A_X/A_V value in a given filter decreases as the filter's central wavelength increases. This is expected for black-body analogues (see Equation 1.8 and Figure 1.1). Both trends are also consistent with the known short-wavelength preference of physical mechanisms causing interstellar extinction.

The accuracy of these relatively simple functions is important because the A_X/A_V dataset for each filter is now reduced to a much smaller number of degrees of freedom, equal to the number of coefficients in the relevant function. The input parameters (T_{eff} , $\log(g)$ and [Fe/H]) are required, regardless of whether interpolation of the tables of A_X/A_V data or the functions are being employed. ****

Filter	Subfunction (SF) (A_{pow} or A_{exp})	SF Coefficients			T_{min} / K
		a	b	c	
F218W	Equation 3.4	a	b	c	
	Equation 3.5	a	b	c	
	Equation 3.6	a	b	c	
F225W	Equation 3.4	a	b	c	
	Equation 3.5	a	b	c	
	Equation 3.6	a	b	c	
F275W	Equation 3.4	a	b	c	
	Equation 3.5	a	b	c	
	Equation 3.6	a	b	c	
F300X	Equation 3.4	a	b	c	
	Equation 3.5	a	b	c	
	Equation 3.6	a	b	c	

Table 3.2: Coefficient values for non-trivial functions produced for fitting to UV filter data.

3.4 Effect on isochrones

The ATLAS9 metallicity chosen for calculating the fixed-extinction A_X/A_V values to be applied to the isochrone was that which best matched the metallicity of the isochrone to which the coefficient was applied. The ATLAS9 value will be denoted $[\text{Fe}/\text{H}]_{CM}$. The first value was equal to $(A_X/A_V)_{\text{plat}} = (A_X/A_V)(T_{\text{eff}} = 50,000\text{K}, \log(g) = 5.0, [\text{Fe}/\text{H}]_{CM})$, and the second was equal to $(A_X/A_V)_{MS} = (A_X/A_V)(T_{\text{eff}} = 5,000\text{K}, \log(g) = 5.0, [\text{Fe}/\text{H}]_{CM})$. This was done to reflect the fact that, for the first case, the assumption of a constant extinction coefficient is valid in the plateau region and, for the second, the fact that, given the position of the MSTO in terms of stellar T_{eff} values, it would be more prudent to ensure that the upper main sequences resulting from both approaches to extinction coincide in the CMD, making it easier to see any disagreements in the turn-off ages. For each of these plots, A_V was fixed at a value of 1.0.

3.4.1 ACS

The CMD chosen for the ACS was the F435W-(F435W-F814W) axis combination. This CMD is useful as it pairs the bluest and reddest wide-field filters for the ACS in its colour index, which is the index most likely to distinguish between objects with a large range of effective temperatures, making it useful for modelling the main sequence and MSTO, the two most important CMD components for calculating cluster isochrone ages. This CMD corresponds, by design, to the pre-existing Johnson-Cousins $B-(B-I)$ CMD (Sirianni et al., 2005), which allows direct comparison of observed data with archive data obtained before the creation of the HST filters.

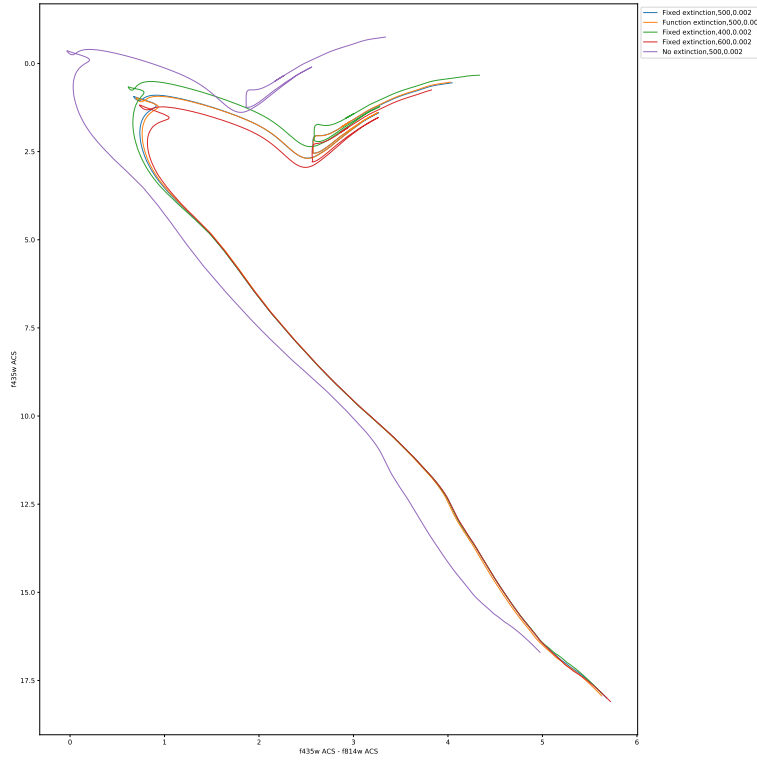


Figure 3.3: ACS F435W-(F435W-F814W) CMD with a fixed extinction ratio equal to $(A_X/A_V)_{MS}$ for each filter

It can be seen in Figure 3.3 that the impact of changing the extinction approach used to change the isochrone position in this CMD is insignificant. Although there are some larger differences in the position of the isochrone in the post-SGB evolutionary stages, this is irrelevant when determining the isochrone age of an observed stellar population.

The result of using $(A_X/A_V)_{plat}$ is not significantly different from that of using $(A_X/A_V)_{MS}$ for this CMD. It can be seen that any changes in A_X/A_V values in the F435W and F814W ACS filters at different temperatures (see Figure 3.2) are insignificant compared to the range of magnitudes covered by the isochrones in Figures 3.3 and 3.4.

3.4.2 WFC3

Two different CMDs were chosen whose filters are part of the WFC3. The first CMD is the F555W-(F555W-F814W) axis combination. This CMD pairs a wide yellow filter (F555W) with the WFC3's reddest IR wide-field filter. This CMD mimics the pre-

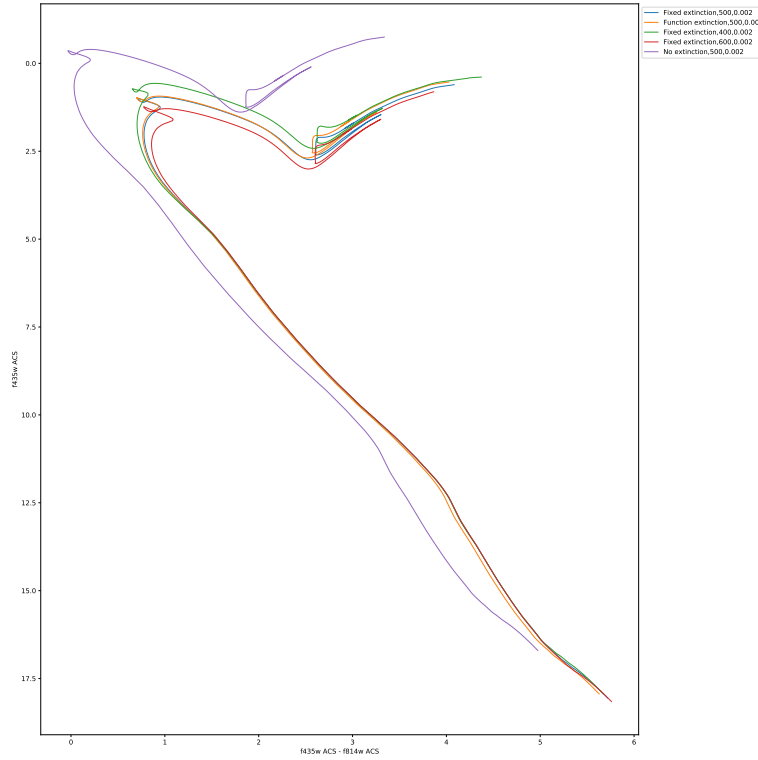


Figure 3.4: ACS F435W-(F435W-F814W) CMD with a fixed extinction ratio equal to $(A_X/A_V)_{plat}$ for each filter

existing and widely-used Johnson-Cousins $V-(V-I)$ CMD (Sahu et al., 2014), which allows direct comparison of observed data with archive data obtained before the creation of the HST filters.

In Figure 3.5, it can be seen that, when the upper main sequences

The second WFC3 CMD that was studied is the F814W-(F275W-F814W) axis combination. The filters that form this CMD cover the soft-UV and near-IR regions of the EM spectrum. The high baseline wavelength coverage of this combination of filters makes the colour index sensitive to differences in T_{eff} in the hot horizontal branch (HB) stars. These objects are important due to direct helium abundance measurements (from absorption lines) being available in globular clusters only for HB stars with $8000 \text{ K} \lesssim T_{\text{eff}} \lesssim 11500 \text{ K}$ (Lagioia et al., 2018).

3.4.3 Gaia

The photometric filters in Gaia, as shown by their respective response functions in Figure 2.2, are designed such that the only reasonable colour index is the $(G_{\text{bp}} - G_{\text{rp}})$ index. The G filter, being the widest filter of the three available wide-field filters. This

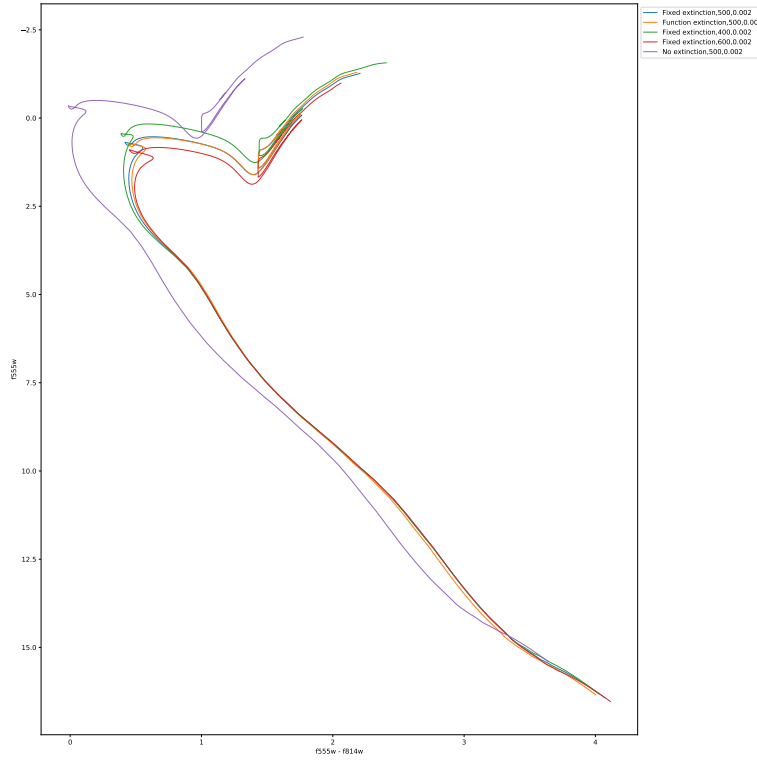


Figure 3.5: WFC3 F555W-(F555W-F814W) CMD with a fixed extinction coefficient equal to $(A_X/A_V)_{MS}$ for each filter

CMD is useful as it pairs the bluest and reddest wide-field filters for the ACS, which produces larger spectral colours.****

3.5 NGC 6793

The Gaia observational dataset of stars in NGC 6793 is shown as a distance-corrected CMD in Figure 3.11, with distances and photometric errors propagated directly from parallax measurements.

Looking at the distances to the objects in the final dataset, it is clear that there are significant variations in the observed parallaxes of individual stars, far beyond the maximum cluster radii expected for the largest open clusters, given as 16.8 ± 2.4 pc by Schilbach et al. (2006) or even radii of compact stellar associations, given as 33.2 ± 21.7 pc in the same paper. Even the . Some objects in the original dataset (338 members in total) were even assigned negative parallax values, which are mathematically impossible. Figure 3.12 shows a histogram of the final NGC 6793 sample****. It is clear that a substantial fraction of this sample have measured parallax distances which put them outside the physical limits of better-studied open clusters.

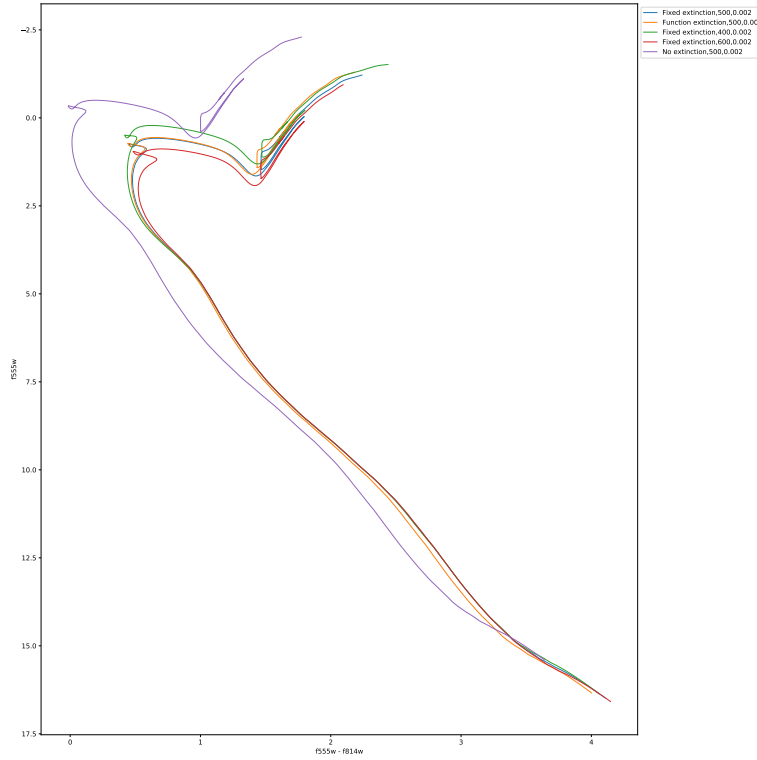


Figure 3.6: WFC3 F555W-(F555W-F814W) CMD with a fixed extinction coefficient equal to $(A_X/A_V)_{plat}$ for each filter

However, ***the errors in the parallax data for objects assigned to NGC 6793 were significant, particularly for stars in the lower main-sequence - understandably, since they are the faintest objects in the data and therefore are more difficult to track against background light sources. The significance persists despite this project assuming that the only source of photometric error is the parallax measurements. This leads to errors in the predicted $M_{\text{ext},X}$ magnitudes, which are calculated by rearranging Equation 1.4. The resulting errorbars are shown in Figure 3.11. The magnitudes of the errorbars dwarf any isochrone position changes due to differing extinction treatments in the lower main sequence. The uncertainties also render differences in position between isochrones with similar parameters insignificant.

Since the table of photometric fluxes did not include photometric errors, the parallax errors alone accounted for the total error in the calculated $M_{\text{ext},X}$. Therefore, the errors on the flux measurements were exactly equal in all filters for a given star. The errors on the $(G_{\text{bp}} - G_{\text{rp}})$ color index were calculated as standard, by adding the individual filter errors in quadrature, giving the color errors which were a factor of $\sqrt{2}$ greater than those for the individual filter fluxes.

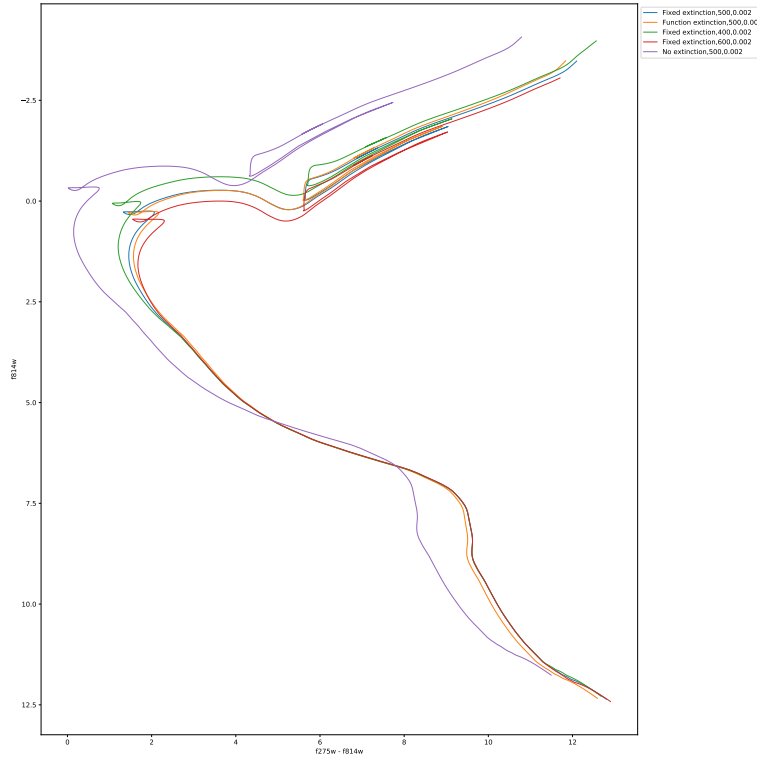


Figure 3.7: WFC3 F814W-(F275W-F814W) CMD with a fixed extinction coefficient equal to $(A_X/A_V)_{MS}$ for each filter

All the isochrones, as shown in Section****, are sensitive both to the reference extinction coefficient value A_V and to the value of A_X/A_V for the fixed-coefficient case, which is to be expected. Some individual parts of the isochrones relevant to this study are additionally sensitive to other isochrone parameters:

1. The position of the MSTO is sensitive to the treatment of A_X/A_V , as shown in Section****, and the isochrone age.
2. The position of the lower main sequence is significantly more sensitive to metallicity than other parts of the isochrone.

Before comparisons with the GC18 parameters can be made, a reference isochrone, with a globally-fixed A_X value of 0.843 and age of 600 Myr (in accordance with Table 2.4), was made. The A_X/A_V values required to achieve alignment with the upper main sequence were equal to the $(A_X/A_V)_{plat}$ values for each Gaia filter. While the results from GC18 do not include a metallicity estimate for NGC 6793, it can be estimated from its age that a solar-like metallicity is likely. Therefore, the relevant isochrone has a metallicity of $[Fe/H] = 0$. Due to the overall red-ward shift of the isochrone caused by

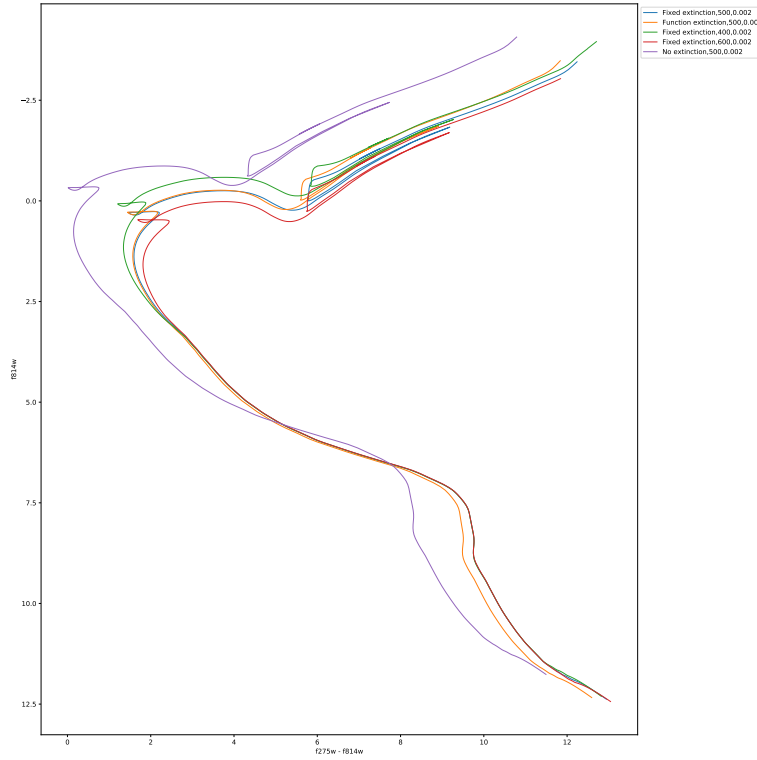


Figure 3.8: WFC3 F814W-(F275W-F814W) CMD with a fixed extinction coefficient equal to $(A_X/A_V)_{plat}$ for each filter

using $(A_X/A_V)_{plat}$, as demonstrated in Figure 3.10, the GC18 parameter values do not apply when using model functions to simulate isochrone extinction. The alignment of the upper main sequence was achieved using a value of $A_V = 1.1$. The best-fit MSTO of this isochrone had an age of 500 Myr. To better align the lower main sequence, an increase in isochrone metallicity was required. The best-fit metallicity was $[\text{Fe}/\text{H}] = 0.062$.

A potential source of uncertainty when comparing the best-fit isochrone results of this project for NGC 6793 with those from GC18**** comes from the fact that this project employs the latest BaSTI isochrone database (Hidalgo et al., 2018), while GC18 uses the PARSEC isochrone database (Marigo et al., 2017). The use of different isochrone software could impact the validity of comparing the A_V values, ages and metallicities arising from both extinction treatments.

Gontcharov et al. (2019) carried out a detailed set of observations of the Galactic globular cluster NGC 5904 in 29 photometric bands. The CMDs created from this data were used to fit isochrones from five different databases, including PARSEC and BaSTI. They adopted the Cardelli et al. (1989) extinction law with the parameters having values of $R_V = 3.60 \pm 0.05$ and $A_V = 0.20 \pm 0.02$. As shown in Table 3.4, the

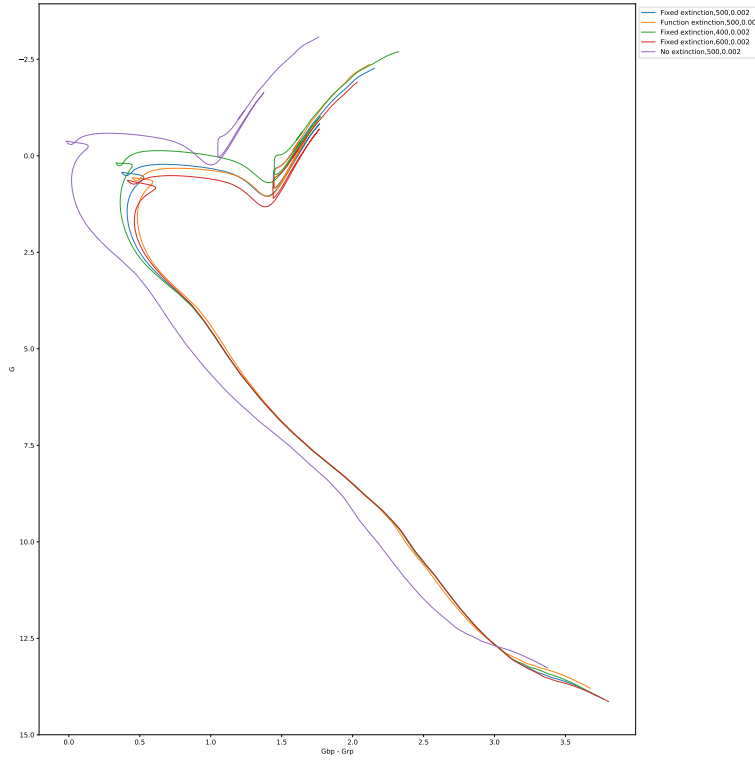


Figure 3.9: Gaia $G-(G_{\text{bp}}-G_{\text{rp}})$ CMD with a fixed extinction coefficient equal to $(A_X/A_V)_{MS}$ for each filter

Gaia colour excess $E(G_{\text{bp}} - G_{\text{rp}})$ for NGC 5904 differs significantly between the best-fits from the two databases, which in turn causes disagreements for the projected cluster age and (photometric) distance. Across all filter systems and isochrone databases, the authors calculated mean estimates of the cluster properties and found that the resulting photometric distance to be in agreement with the cluster distance calculated from the Gaia parallaxes of the cluster members.

In the case of the analysis of NGC 6793 made here, the distance measurements are derived from parallax measurements and so are unaffected by the choice of isochrone software, allowing the GC18 cluster distance to be assumed here (as 600 pc to the cluster centre). Furthermore, using the PARSEC-derived parameters from GC18, an accurate BaSTI model isochrone was nevertheless produced successfully without any deviation from standard assumptions made for an extinction model of constant A_X/A_V .

Therefore, it was concluded that the validity of comparing of the respective A_X , $[\text{Fe}/\text{H}]$ and age values from GC18 and this project was not endangered by the use of different isochrone databases by the each study.

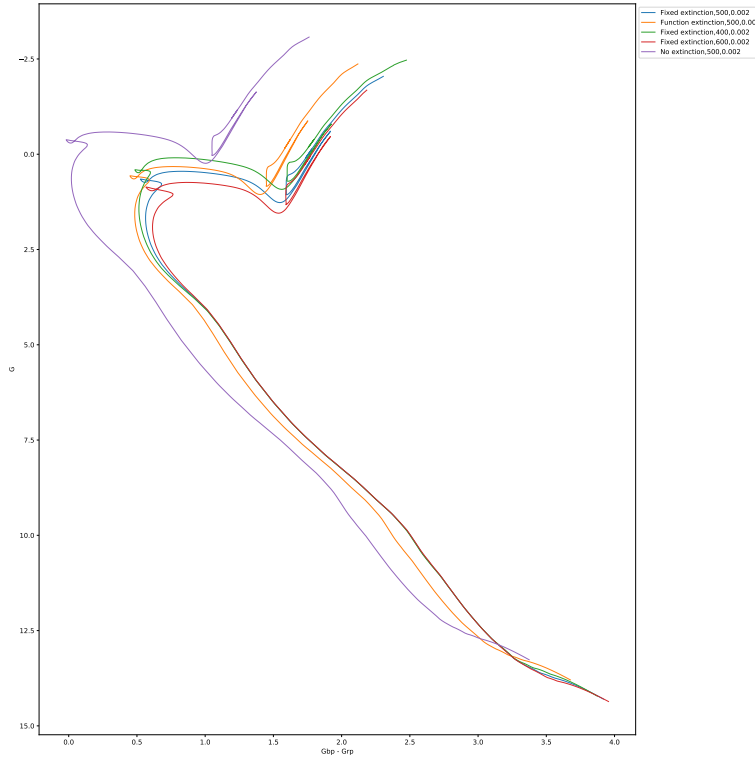


Figure 3.10: Gaia $G-(G_{bp}-G_{rp})$ CMD with a fixed extinction coefficient equal to $(A_X/A_V)_{plat}$ for each filter

As predicted by the comparisons made in Section 3.4.3, the isochrone with a function-based extinction at the GC18 value of $A_V = 0.84$ is systematically too blue and too bright to fit to the observed CMD of NGC 6793. This remains the case regardless of changes in age and metallicity. Therefore, there is significant disagreement between the A_V values between the two extinction calculation methods.****

**** There are considerable uncertainties for the parameters in both isochrones in Figure ****. Most fundamentally, the position of the MSTO is reliant only on the position of the four brightest cluster members, of which the brightest two, if the isochrones are accurate, appear to be part of part of the cluster's SGB hook (Pols et al., 1998). Furthermore, these two hook members are not covered by either isochrone, with the position differences being highly**** significant regarding the objects' (small) parallax errors. This disagreement persists even with substantial changes in metallicity, while any changes in A_V and age cause misalignment with the main sequence and MSTO, respectively.

Cluster property	K05	GC18	This project
Age / Myr	437	603	500
A_V / mag	0.53	0.843	1.1
$[Fe/H]$?	?	0.062
Members	?	271 (photometric)	274

Table 3.3: Comparison of results from this project with observational parameters for NGC 6793 from Table 2.4

Cluster property	PARSEC	BaSTI
$E(G_{bp} - G_{bp})$ / mag	0.080 ± 0.02	0.013 ± 0.03
Age / Gyr	11.5	12.5
Distance / pc	7600	8400

Table 3.4: Comparison of best-fit parameter results for NGC 5904 using PARSEC and BaSTI. Data taken from Gontcharov et al. (2019).

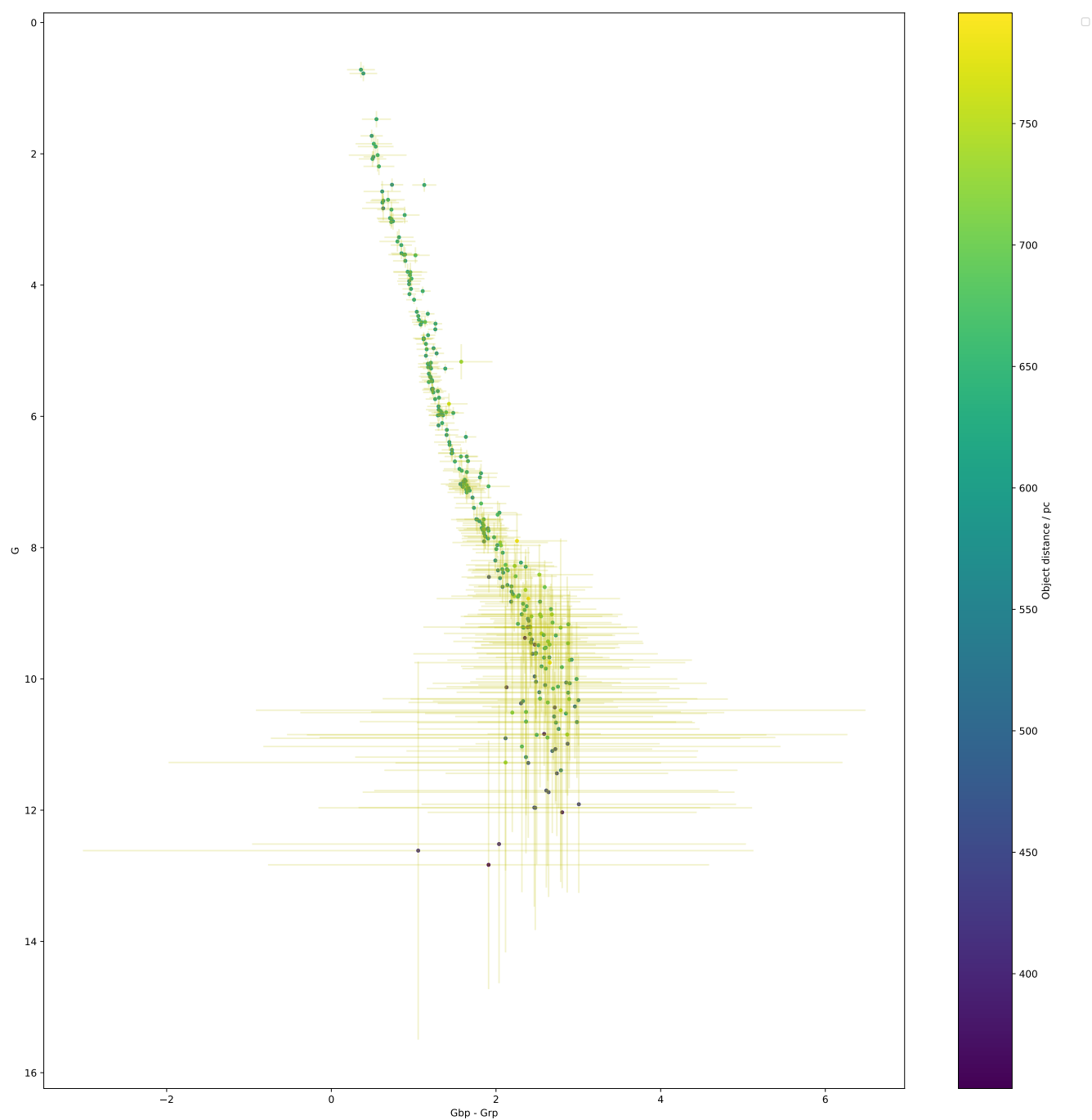


Figure 3.11: Gaia G -(G_{bp} - G_{rp}) CMD showing the 274 cluster members in the final dataset, with errorbars added. The color of each object is determined by its parallax-derived distance.

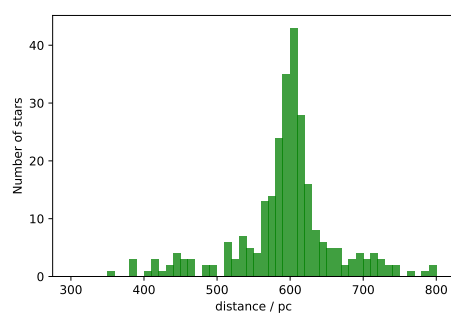


Figure 3.12: Histogram of distances for the 274 stars in the final observational dataset. The bins are set to a fixed width of 10 pc.

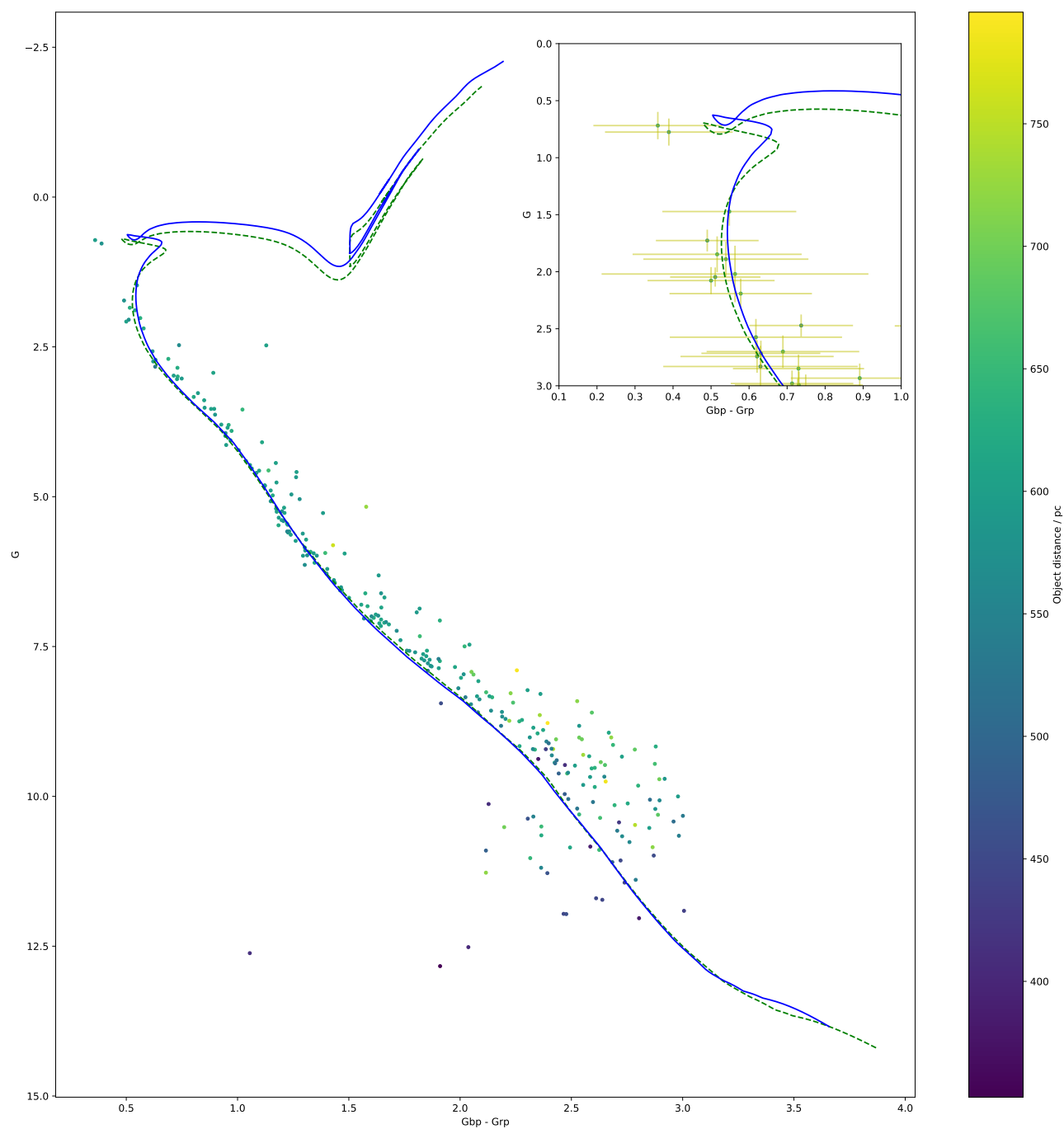


Figure 3.13: ****Gaia $G-(G_{bp}-G_{rp})$ CMD showing the 274 cluster members in the final dataset, with errorbars shown. The color of each object is determined by its parallax-derived distance.

Chapter 4

Conclusion & future work

In all cases, applying a fixed extinction to all points in an isochrone causes the main-sequence turn-off to occur at a more luminous, bluer point in a given CMD than the MSTO point for an isochrone with extinction values for every star described using an analytical function fitted to empirically-derived data.

The significance of this position change is dependent on the filters used to construct the CMD in question. The position changes in the HST ACS and WFC3 systems' CMDs are insignificant. The Gaia photometric CMD, by contrast, is highly sensitive to the A_X values applied to the filters. This applies not only when comparing the fixed- A_X/A_V approach to the function approach, but also when comparing the fixed approaches using $(A_X/A_V)_{plat}$ and $(A_X/A_V)_{MS}$. This underscores the risk of incorrect assumptions being made when fitting isochrones to observational data with globally-fixed (A_X/A_V) ****

4.1 Future work

There are multiple ways to extend the applicability of the work done in this project. The most obvious example is to acquire and utilise the response functions of more filter systems, particularly for more modern and more sensitive instruments, such as the James Webb Space Telescope (JWST) and the proposed WFIRST and PLATO space telescopes.

Another extension would be to apply the function-based extinction approach to observed clusters with isochrone ages determined using the globally-fixed A_X approach. If, as predicted for the limited examples studied in this project, the isochrone ages of a given cluster CMD are greater when employing a fixed-extinction approach, there is the possibility of a systematic decrease in the predicted ages of these observed after comparison with ages derived using a function-based approach.

Regarding the case of NGC 6793, follow-up observations with Johnson-Cousins

filters, if feasible, could resolve the A_V disagreement between extinction-calculation methods by providing a direct measured value upon which the Gaia extinction ratios can be calculated.

Finally, the limits on the accuracy of the model functions presented here require investigation, particularly the accuracy limit at the lowest T_{eff} values available from ATLAS9. This could be done using the same approach as that used by Girardi et al. (2008), who use models from **** to extend their bolometric correction database to a minimum T_{eff} of 1000 K. The coolest known stellar objects (excluding brown dwarfs) have $T_{\text{eff}} \gtrsim 2500$ K. Extending the dataset would constrain the allowed behaviour of the model functions in the lowest ATLAS9 metallicities. Currently, the lack of data below 3500 K prevents investigation of the significance of the tail-flick phenomenon, since the phenomenon, at present, extends to (and possibly beyond) the lower- T_{eff} limit for the affected filters.

Bibliography

- Bessell M. S., 1990, *PASP*, 102, 1181
- Cardelli J. A., Clayton G. C., Mathis J. S., 1989, *ApJ*, 345, 245
- Casagrande L., VandenBerg D. A., 2014, *MNRAS*, 444, 392
- Casagrande L., VandenBerg D. A., 2018, *MNRAS*, 479, L102
- Castellani V., Chieffi A., Straniero O., 1992, *ApJS*, 78, 517
- Castelli F., Kurucz R. L., 2004, *ArXiv Astrophysics e-prints*
- Fitzpatrick E. L., 1999, *PASP*, 111, 63
- Forbes J. D., 1842, *Philosophical Transactions of the Royal Society of London Series I*, 132, 225
- Gaia Collaboration et al., 2018, *A&A*, 616, A10
- Girardi L., Bertelli G., Bressan A., Chiosi C., Groenewegen M. A. T., Marigo P., Salasnich B., Weiss A., 2002, *A&A*, 391, 195
- Girardi L., et al., 2008, *PASP*, 120, 583
- Gontcharov G. A., Mosenkov A. V., Khovritchev M. Y., 2019, *MNRAS*, 483, 4949
- Gustafsson B., Edvardsson B., Eriksson K., Jørgensen U. G., Nordlund Å., Plez B., 2008, *A&A*, 486, 951
- Hidalgo S. L., et al., 2018, *ApJ*, 856, 125
- Johnson H. L., Morgan W. W., 1953, *ApJ*, 117, 313
- Jordi C., et al., 2010, *A&A*, 523, A48
- Kalirai J. S., Baggett S., Borders T., Rajan A., 2010, Technical report, The Photometric Performance of WFC3/UVIS: Temporal Stability Through Year 1
- Kharchenko N. V., Piskunov A. E., Röser S., Schilbach E., Scholz R.-D., 2005, *A&A*, 438, 1163

- Kurucz R., 1993, ATLAS9 Stellar Atmosphere Programs and 2 km/s grid. Kurucz CD-ROM No. 13. Cambridge, Mass.: Smithsonian Astrophysical Observatory, 1993., 13
- Lagioia E. P., et al., 2018, MNRAS, 475, 4088
- MacKenty J. W., Kimble R. A., O’Connell R. W., Townsend J. A., 2010, in Space Telescopes and Instrumentation 2010: Optical, Infrared, and Millimeter Wave. p. 77310Z
- Marigo P., et al., 2017, ApJ, 835, 77
- O’Donnell J. E., 1994, ApJ, 422, 158
- Ohvri H., Okulov O., Teral H., Teral K., 1999, Solar Energy, 66, 305
- Paczynski B., Stanek K. Z., 1998, ApJ, 494, L219
- Pietrinferni A., Cassisi S., Salaris M., Castelli F., 2004, ApJ, 612, 168
- Pols O. R., Schröder K.-P., Hurley J. R., Tout C. A., Eggleton P. P., 1998, MNRAS, 298, 525
- Rieke G. H., Lebofsky M. J., 1985, ApJ, 288, 618
- Sahu K., Deustua S., Sabbi E., 2014, Technical report, WFC3/UVIS Photometric Transformations
- Sarajedini A., et al., 2007, ApJ, 133, 1658
- Schilbach E., Kharchenko N. V., Piskunov A. E., Röser S., Scholz R.-D., 2006, A&A, 456, 523
- Sirianni M., et al., 2005, PASP, 117, 1049
- Valencic L. A., Clayton G. C., Gordon K. D., 2004, ApJ, 616, 912